

Three-Dimensional Self-Assembled Photonic Crystal Waveguide

A DISSERTATION
SUBMITTED TO THE FACULTY OF THE GRADUATE SCHOOL
OF THE UNIVERSITY OF MINNESOTA
BY

Kang-Hyun Baek

IN PARTIAL FULFILLMENT OF THE REQUIREMENTS
FOR THE DEGREE OF
DOCTOR OF PHILOSOPHY

Anand Gopinath

December 2010

© Kang-Hyun Baek 2010

Acknowledgements

I would like to thank my advisor, Professor Anand Gopinath, for his academic advice, support, and encouragement throughout the course of my study and work. Without his guidance, this work would not have been possible.

I would like to thank Prof. James Leger, Prof. Bethanie Stadler, Prof. Paul Crowell, and Prof. David Norris for serving on my preliminary and final oral exam committee and reviewing the manuscript of my dissertation.

I would like to thank all members of Prof. Gopinath's research group, my research coworkers, and my fellow students for their valuable discussion and assistance: William Berglund, Prakash Koonath, Chanin Laliew, Ross Schermer, Danial Olson, Aaron Christmann, Dr. Sun Sook Lee, Jang-Uk Lee, Woohyek Choi, Woo-Bin Song, and Sangho Song.

Special thanks are offered to Prof. Dong Myong Kim, my advisor at Kookmin University in Korea, for his guidance and encouragement to continue my studies.

Finally, I would like to express my deepest gratitude to my wife, Hyun-Jung, my parents, Seong-Ki and Yeon-Ok, my parents-in-law, Han-Joo Kim and Un-Ki Kim, my sister, Seung-Hyun, and my paternal aunts, Myong-Im and Yeon-Hwa, for their endless love, support, encouragement and sacrifice.

Abstract

Photonic crystals (PCs), two- or three-dimensionally periodic, artificial, and dielectric structures, have a specific forbidden band for electromagnetic waves, referred to as photonic bandgap (PBG). The PBG is analogous to the electronic bandgap in natural crystal structures with periodic atomic arrangement. A well-defined and embedded planar, line, or point defect within the PCs causes a break in its structural periodicity, and introduces a state in the PBG for light localization. It offers various applications in integrated optics and photonics including optical filters, sharp bending light guides and very low threshold lasers. Using nanofabrication processes, PCs of the 2-D slab-type and 3-D layer-by-layer structures have been investigated widely. Alternatively, simple and low-cost self-assembled PCs with full 3-D PBG, inverse opals, have been suggested. A template with face centered cubic closed packed structure, opal, may initially be built by self-assembly of colloidal spheres, and is selectively removed after infiltrating high refractive index materials into the interstitials of spheres.

In this dissertation, the optical waveguides utilizing the 3-D self-assembled PCs are discussed. The waveguides were fabricated by microfabrication technology. For high-quality colloidal silica spheres and PCs, reliable synthesis, self-assembly, and characterization techniques were developed. Its theoretical and experimental demonstrations are provided and correlated. They suggest that the self-assembled PCs with PBG are feasible for the applications in integrated optics and photonics.

Table of Contents

List of Figures	v
Chapter 1: Introduction	1
Chapter 2: Numerical Simulations & Design	3
2.1 Introduction	3
2.2 Photonic band structure of opal & inverse opals	5
2.3 Photonic band structure of self-assembled PCs with defect	8
2.4 Spectral characteristics of self-assembled PC waveguide	12
2.4.1 Finite difference time domain (FDTD) simulation	12
2.4.2 Results and discussion	15
Chapter 3: Self-Assembled Photonic Crystals	21
3.1 Introduction	21
3.2 High-quality monodisperse silica spheres	22
3.2.1 Stöber-Fink-Bohn method	22
3.2.2 Seeded growth technique	24
3.2.3 Preparing monodisperse single-spheres	27
3.2.4 Efficient fast growth method	29
3.2.5 Shrink-proof spheres	32
3.3 Self-assembly & inverting processes	35
3.3.1 Convective self-assembly method	36

3.3.2 Assisted convective-method by the Marangoni effect	37
3.3.3 Amorphous silicon inverse opals	40
3.4 Optical characterizations by FTIR spectroscopy	43
Chapter 4: Self-Assembled Photonic Crystal waveguides	47
4.1 Introduction	47
4.2 Opal-clad optical waveguide	48
4.2.1 Rib-type waveguide structure	49
4.2.2 Micro-fabrications & SEM characterizations	51
4.2.3 Optical characterizations	54
4.2.3.1 Propagation loss measurements	54
4.2.3.2 Transmission spectrum measurement	57
4.3 Embedded defect structures in α -Si inverse opals	59
4.3.1 Planar-defect Si_3N_4 layer	60
4.3.2 Line-defect α -Si waveguide	63
Chapter 5: Conclusions and Future Works	68
Bibliography	70

List of Figures

Figure 2.1: Schematic of opal with <i>fcc</i> closed-packed arrangement and its primitive unit cell used in PWE calculation.	4
Figure 2.2: Photonic bandstructure of opal.	5
Figure 2.3: Photonic bandstructure of inverse opal.	6
Figure 2.4: Schematics of Si-waveguide embedded in inverse opal and supercell with a defect.	8
Figure 2.5: PWE calculation results using supercell method.	9
Figure 2.6: Bandstructure of the supercell with defect within the PBG and electric field distributions of some selected defect modes.	11
Figure 2.7: Schematic of self-assembled PC waveguide with a rectangular Si-guide defect and the used computational domain, transmitted power spectra, and propagation losses at $\lambda=1550$ nm depending on domain size.	13
Figure 2.8 Transmitted power spectra depending on propagation distance of $z=0\sim 16.5\ \mu\text{m}$.	16
Figure 2.9: Propagation losses in dB/100 μm at several selected wavelengths of inside, outside, and edge stopband.	18
Figure 2.10: Band structure and power spectrum of the inverse opal with a Si-guide defect	19

Figure 3.1: Measured diameters and calculated volumes of silica sphere synthesized by Stöber-Fink-Bohn method as a function of reaction time.	23
Figure 3.2: Schematic growth profile of silica spheres in seeded growth technique.	25
Figure 3.3: Diameters and standard deviations of silica spheres obtained by seeding growth technique.	26
Figure 3.4: SEM images of silica spheres containing 8.8 % and 3.0 % aggregates, schematic of singles collection technique, and SEM image of 0.3 % aggregates after centrifuge collection.	28
Figure 3.5: Schematic and actual growth profiles of the modified seeded method and the conventional one.	30
Figure 3.6: SEM image of silica spheres containing aggregates of 0.6 %.	32
Figure 3.7: Thermal shrinkage of silica spheres.	33
Figure 3.8: Schematic setup diagram of convective capillary meniscus method and SEM top-view image of opals.	36
Figure 3.9: Marangoni effect in the aqueous 1-propanol mixture, surface tensions and boiling points of the mixture depending on compositions in liquid phase, and phase diagram of the mixture.	38
Figure 3.10: SEM top-view images of self-assembled opal with different magnifications.	40
Figure 3.11: Schematics of opal inverting processes.	41

Figure 3.12: SEM images of self-assembled inverse opals with <i>fcc</i> closed-packed structure.	42
Figure 3.13: FTIR spectroscopy results of opals.	44
Figure 4.1: Schematic of opal-clad Si ₃ N ₄ waveguide and mode profile calculated by imaginary distance beam propagation method.	48
Figure 4.2: Leakage loss analysis of the planar multilayer structure using transfer matrix technique.	50
Figure 4.3: Opal-clad waveguide fabrication processes.	52
Figure 4.4: Cross sectional SEM images of the opal-clad waveguides.	53
Figure 4.5: Propagation loss measurement results depending on the width and length of rib waveguide.	55
Figure 4.6: Measured propagation losses of the opal-clad waveguide.	56
Figure 4.7: Measured transmission spectrum of opal-clad waveguide, and calculated spectrum by 2-D simulation using imaginary distance beam propagation technique.	58
Figure 4.8: Schematics of embedded defect structures in α -Si inverse opals.	60
Figure 4.9: Fabrication process flow of planar defect.	61
Figure 4.10: SEM images of a planer defect embedded in the inverse opals.	62
Figure 4.11: Schematics of the fabrication process flow.	64

- Figure 4.12: Schematic and SEM image of self-assembled silica spheres on a line-defect. 65
- Figure 4.13: Schematic and SEM image of the completely released opal membrane and an inserted line defect and confocal microscopic images of 2-D top-view and 3-D geometry. 66
- Figure 4.14: Schematic and SEM top-view image of the fabricated α -Si waveguide embedded within the inverse opals. 67

Chapter 1: Introduction

Photonic crystal (PC) is an artificial structure with periodic arrangement of materials with dielectric contrast, which leads to photonic bandgaps (PBGs) where light at the specific frequencies is evanescent. The PBG enables the spontaneous emission control and the localization of photons in any defect [1]-[3]. It has been therefore studied widely for various practical applications in nano-photonics and optics to utilize the unique optical properties [4]-[6]. Three-dimensional (3-D) PC using a self-assembly technique, the inverse opal, has attracted significant interest [7]-[9]. A self-assembled face centered cubic closed-packed structure of silica spheres, the opal, is employed as a template to be removed after infiltrating a high dielectric material into its pores (i.e. inverse opal). The studies on self-assembled PC waveguide for air light-guide have been recently reported as attempts to incorporate the complete PBG into compact photonic devices [10]-[12].

In this dissertation, the embedded defects in 3-D self-assembled PCs and their applications are discussed. In Chapter 2, photonic bandstructure of the self-assembled PCs is calculated by the plane wave expansion (PWE) method and utilized for waveguide design. For practical applications near 1550 nm in wavelength, 3-D Finite difference time domain (FDTD) simulations are performed, and its unique properties and performance are characterized and evaluated. In Chapter 3, the fabrication of self-assembled PCs (opal and inverse opal) is discussed with theoretical and experimental justification. Initially, large monodispersed, shrink-proof, and high-purity colloidal silica

spheres are prepared through efficient fast-growth, preannealing, and centrifuge collection process. Self-assembled PCs are built by convective method assisted by the Marangoni effect and characterized by SEM inspection and FTIR spectroscopy. In Chapter 4, practical self-assembled PC applications incorporated with several defect structures are proposed and fabricated. First, opal-clad Si_3N_4 waveguide was fabricated and characterized, and its theoretical and experimental results were compared. Next, embedded planar- and line-defect waveguides in inverse opals were built by microfabrication process technology including micro-electro-mechanical systems (MEMS) fabrication technique, and their SEM characterizations are discussed. In Chapter 5, the overall work in this dissertation is summarized and future work has been suggested.

Chapter 2: Numerical Simulation & Design

2.1 Introduction

The artificial 3-D PC may lead to a complete PBG due to the omnidirectional periodic structure with the dielectric contrast, which enables control of electromagnetic waves within specific frequency bands. To understand their physical behavior and exploit their unique properties, various numerical calculations have been performed by several computational techniques, e.g., plane wave expansion (PWE) method [3], [7], [13]-[19], transfer matrix method [20]-[23], finite difference time domain (FDTD) method [24]-[28], etc.

In this chapter, the PWE and FDTD method are employed to investigate and design the embedded waveguide in the 3-PCs, for which the simulation programs are provided by Rsoft Design Group, Inc. and MIT Photonic Bands (MPB) Package [29]-[31]. The simple, reliable, and most commonly used PWE method (frequency domain) is able to solve the Maxwell's equations over a periodic geometry formulated as a linear eigenvalue problem. The modal solutions corresponding to all crystal directions constitute the photonic bandstructure of the PC, which contains useful information to characterize and design the periodic structure including spectral position of the PBG, field distributions of the mode, lattice constant of the PC, etc. This approach is applied to the 3-D PC waveguide structure as well, where the periodicity is essentially broken due to an introduced waveguide defect [32]-[36]. From this band calculation of PC

waveguide, guided defect modes may be defined, which exist in the PBG and are localized at the defect.

For studying the distinctive features of the realistic PC waveguide, the 3-D FDTD simulations were used. The FDTD technique is able to directly solve Maxwell's curl equations in the time domain on a space grid [25], [37]. The calculated time-varying response may be Fourier-transformed for spectral characterizations via transmitted power and propagation loss spectra. Light signals of the stopband associated with guided defect modes may be confined and transmitted through the defect, and the defect may split the original PC stopband into local pass- and stop-bands. In Section 2.4.2, the simulation results obtained from the PWE and FDTD techniques are compared.

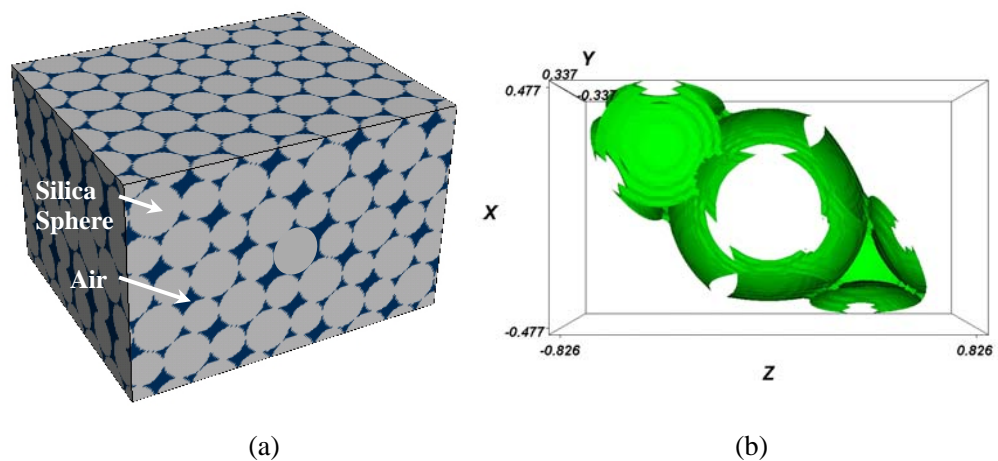


Figure 2.1 Schematic of opal with *fcc* closed-packed arrangement (a), and primitive unit cell (parallelepiped) used in PWE calculation (b): It is a composite material of silica spheres with a refractive index (n) of 1.45 and interstitial air with n of 1.0.

2.2 Photonic band structure of opal & inverse opals

The opal with a face centered cubic (*fcc*) closed-packed structure is a composite material of silica spheres ($n=1.45$) and interstitial air ($n=1.0$), as shown in Figure 2.1(a). To define the infinite and perfect crystal for computational purposes, a primitive unit cell is specified and periodic conditions are applied to the cell boundaries from the Bloch's theorem. A parallelepiped of Figure 2.1(b) represents the unit cell of perfect crystalline opal used in this calculation. The calculated bandstructure is shown in Figure 2.2 in which the lines (bands) represent the modal solutions (modes) of Maxwell's equation obtained by the PWE method. The a/λ is a dimensionless and normalized

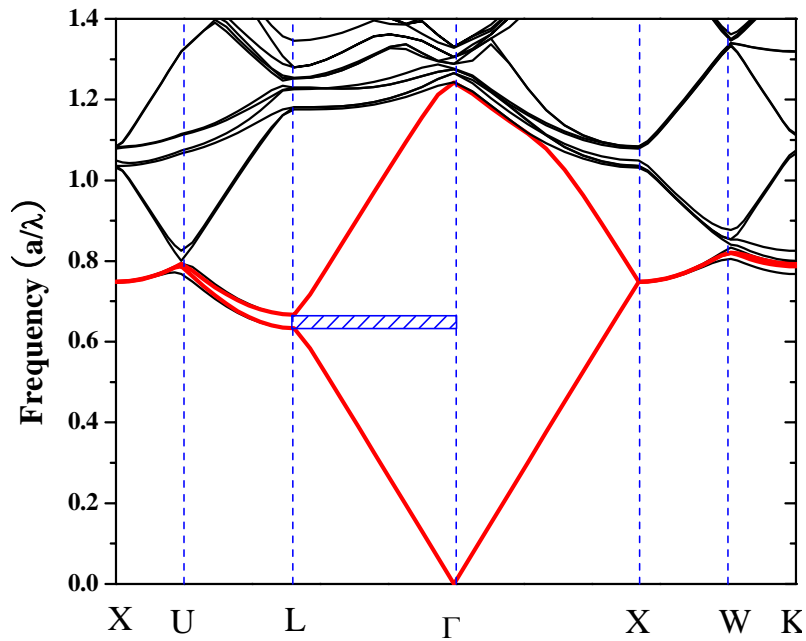
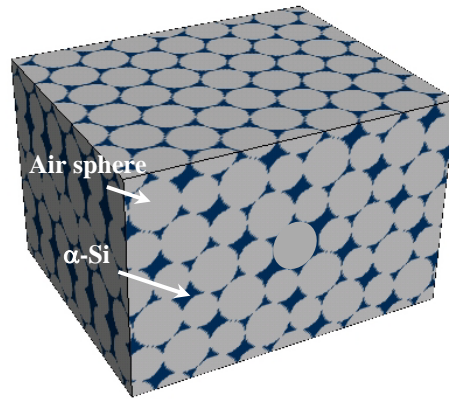
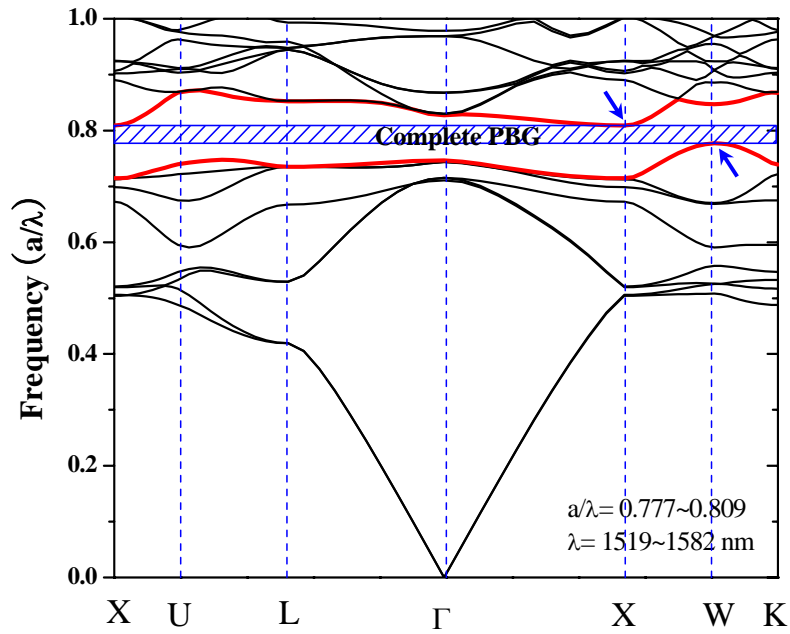


Figure 2.2 Photonic bandstructure of opal calculated by PWE method: The hatched area represents a bandgap with bandwidth of 5.1% placed in Γ -L direction and at $a/\lambda= 0.634\sim 0.667$.



(a)



(b)

Figure 2.3 Photonic bandstructure of inverse opal: (a) schematic of inverse opal, which has air spheres with n of 1.0 and infiltrated α -Si with n of 3.48; (b) band structure shows a complete PBG with bandwidth of 4.0 % for $a/\lambda = 0.777 \sim 0.809$ (hatched area).

frequency as a function of reciprocal wave vector in the direction of some symmetry critical points (Γ , L, U, X, W, and K), where a is *fcc* lattice constant and λ is free space

wavelength. A frequency bandgap (mode-free zone) between the 2nd and 3rd bands occurs at $a/\lambda=0.634-0.667$, which we call a pseudo-PBG because it exists only in the Γ -L direction [38]. Its bandwidth ($\Delta(a/\lambda)$) of 5.1 % can be obtained as follows:

$$\Delta(a/\lambda) = 2 \times \frac{(a/\lambda)_{upper,min} - (a/\lambda)_{lower,max}}{(a/\lambda)_{upper,min} + (a/\lambda)_{lower,max}} \quad (2.1),$$

where $(a/\lambda)_{upper,min}$ and $(a/\lambda)_{lower,max}$ are the upper- and lower-edges of PBG (arrows of Figure 2.3(b)).

The band calculation of the inverse opal uses the structure composed of air spheres ($n=1.0$) and interstitial α -Si material ($n=3.48$). A parallelepiped unit cell with periodic boundary conditions is used for the calculation. The calculated photonic bandstructure reveals a complete PBG with the bandwidth of 4.0% placed at $a/\lambda=0.777-0.809$ between 8th and 9th bands, as shown in Figure 2.3(b) and reported in [7], [39].

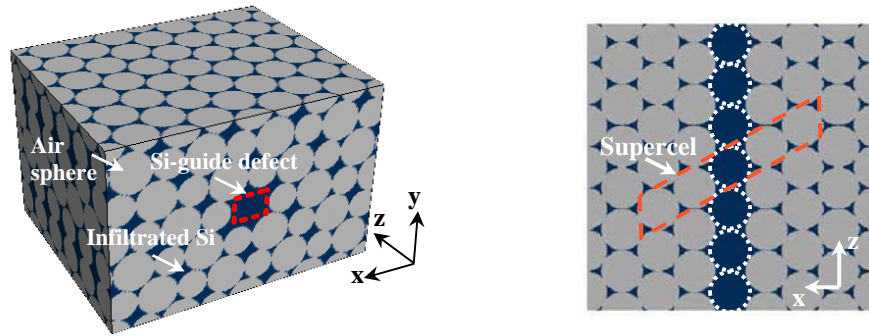
For the realistic PC applications near $\lambda_c=1550$ nm, the respective diameters (D) of the silica and air spheres may be chosen as follows:

$$a/\lambda_c = \frac{\sqrt{2}D}{\lambda_c} \quad (2.2),$$

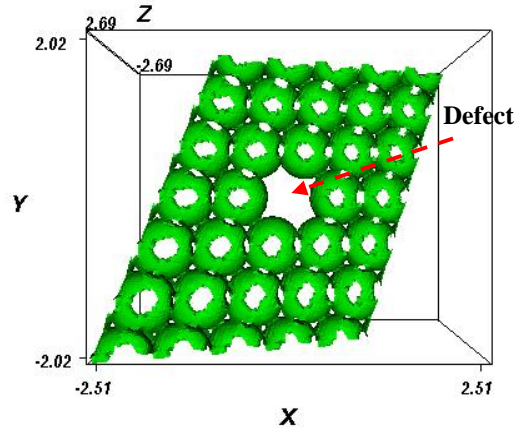
where a/λ_c is a center frequency of PBG and $a=\sqrt{2}D$ is attributed to the *fcc* closed packed structure. The diameters of 713 nm (silica sphere for opal) and 869 nm (air sphere for inverse opal) are obtained, where the corresponding stopbands to the PBGs are 1512~1590 nm and 1519~1582 nm, respectively.

2.3 Photonic band structure of self-assembled photonic crystals with defect

For the band calculation of PCs with a defect as shown in Figure 2.4(a), a new unit cell needs to be defined because of its periodicity disruption. It consists of a centered defect and a multiple of original unit cells, which may be called the supercell [32]-[36]. Applying the identical periodic boundary condition used in the defect-free PC, the overall crystal structure contains an array of defects, and they may interact and couple



(a)



(b)

Figure 2.4 (a) Schematics of the Si-waveguide embedded in inverse opal; (b) supercell (parallelepiped, $5(a/\sqrt{2}) \times 6(a/\sqrt{3}) \times (a/\sqrt{2})$) with a centered defect used in the PWE calculation.

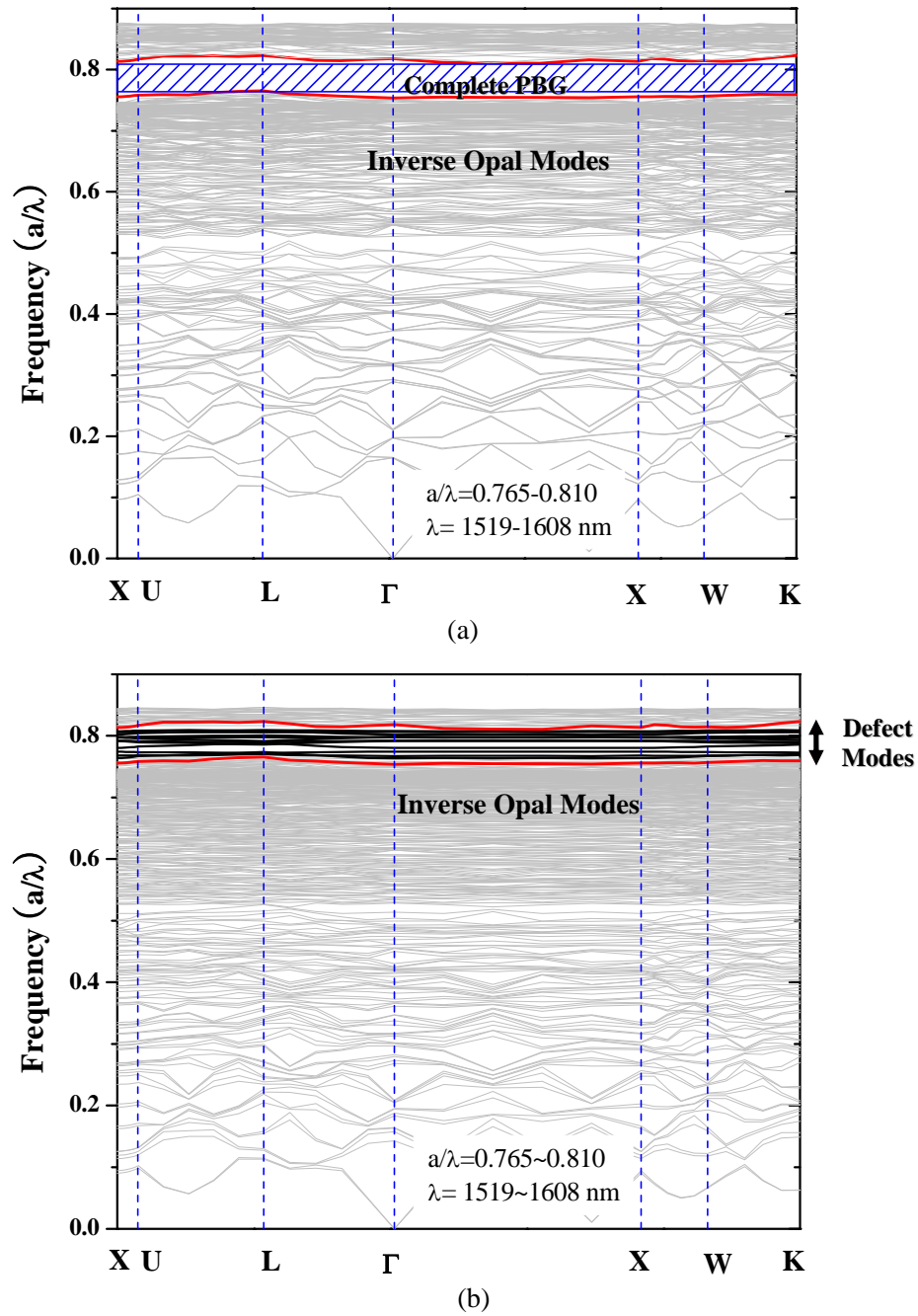
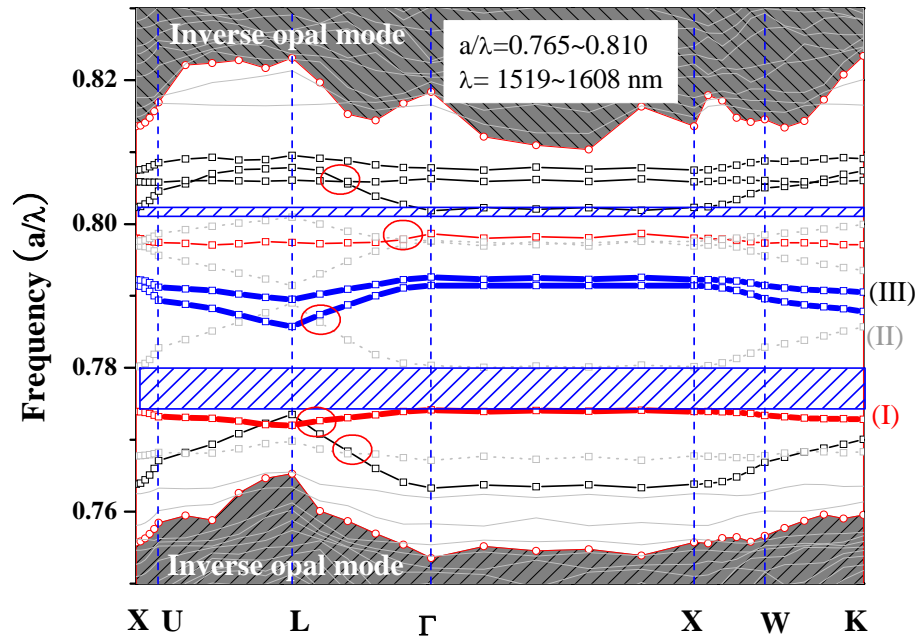


Figure 2.5 Calculation results using supercell method: (a) bandstructure of inverse opal using defect-free supercell: A complete PBG of $a/\lambda = 0.765 \sim 0.810$ (hatched area, bandwidth of 5.7%) is observed; (b) bandstructure of the supercell with waveguide defect (Figure 2.4(b)), which possess several defect bands within the PBG: The obtained bandgap edges from Figure 2.5(a) are used to define PBG.

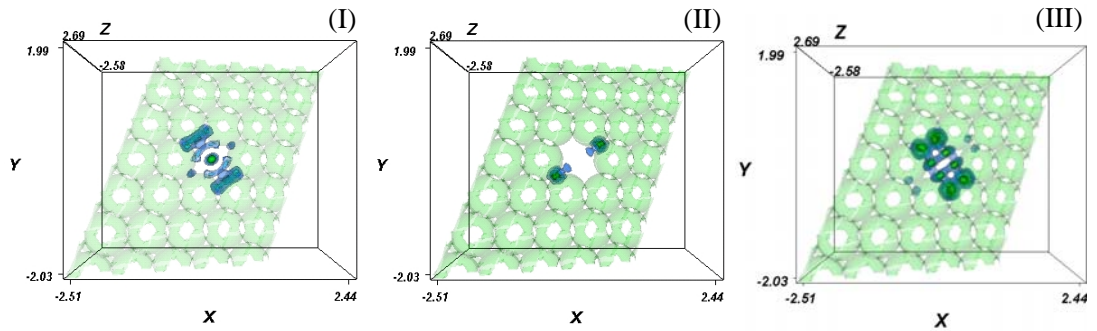
to one another. The sufficient isolation of defects is eventually necessary for the accurate PWE calculation, and it may be formed through the appropriate supercell size taking account of the computational time. Figure 2.4(b) represents the supercell with a centered Si-defect, of which the size is $5(a/\sqrt{2}) \times 6(a/\sqrt{3}) \times (a/\sqrt{2})$.

Initially, a simulation of a defect-free supercell was performed. The complicated bandstructure containing the inverse opal modes (bulk modes or propagating modes into the PC) and a PBG between the 240th and 241st band (edge-bands, red lines) is shown in Figure 2.5(a). The hatched region indicates the PBG, where $a/\lambda = 0.765 \sim 0.810$, bandwidth of 5.7 %, and $\lambda = 1519 \sim 1608$ nm, and it is comparable to the result from the single unit cell calculation. The increased number of bands comes from the 30 times ($5 \times 6 \times 1$) larger cell size compared to the original. The larger the size is, the smaller its Brillouin zone is, and the number of bands increases through band folding, as specified in [3], [29]. Figure 2.5(b) shows the bandstructure for the supercell with defect, where the edge-bands (red lines) of Figure 2.5(a) are projected to define PBG and several defect bands are observed within it. The number of bands below the PBG increased by about 10% over the defect-free case, and it indicates the existence of spurious modes produced by the coupling of defects.

For a detailed analysis of the defect modes, the magnified bandstructure near the PBG is depicted in Figure 2.6(a). Within the PBG, a total of twelve defect bands (square and line, except ones overlapped partially with the edge band), two local bandgaps (hatched area, complete absence of propagation modes), and several crossings of bands (circles, interaction between modes) are observed. The modes are classified by its



(a)



(b)

Figure 2.6 (a) Bandstructure of the supercell with defect within the PBG: Twelve defect bands (square and line, except ones overlapped partially with the edge band), two local bandgaps (hatched area, complete absence of mode), and several crossings of bands (circle) are observed. The bands (modes) were classified by its electric field intensity at the center of defect: high-intensity modes (bold solid lines), moderate-intensity modes (solid lines), and low-intensity modes (dotted lines); (b) electric field distributions of some selected defect modes: (I) high-intensity and center-localized (fundamental) mode, (II) low-intensity and surface-localized mode, and (III) high-intensity and high-order mode.

electric field distribution and intensity at the defect center, and some selected defect modes are shown in Figure 2.6(b). The (I) and (III) of Figure 2.6(b) indicate a center-localized (fundamental) mode and a high-order mode, respectively, which possess high-intensity near the defect center. The (III) is a low-intensity and surface-localized mode (surface-like mode [35]), of which the electric field is mostly confined at the surface of the defect.

In the next section, the distinctive features of bandstructure will be correlated with the waveguide spectral characteristics (i.e. transmitted power and propagation loss spectra) calculated by the finite difference time domain method.

2.4 Spectral characteristics of self-assembled photonic crystal waveguide

2.4.1 Finite difference time domain (FDTD) simulation

Unique spectral characteristics induced by the electro-magnetic behavior of PBG in the PC with embedded waveguide have been investigated using the finite difference time domain (FDTD) method. Transmitted power and propagation loss were calculated as a function of the propagation distance (z). The computational structure consists of air spheres with refractive index (n) of 1.0, infiltrated silicon regions with n of 3.48, and a silicon guide defect, as shown in Figure 2.7(a). The air sphere diameter (D) of 870 nm was chosen to obtain the stopband of 1519~ 1608 nm, as described in Section 2.3. The cross sectional dimensions of a rectangular Si-guide defect enclosed in the air spheres have a width (W) of 0.637 μm and a height (H) of 0.551 μm .

To monitor the power transmitted through the waveguide, some detection plates

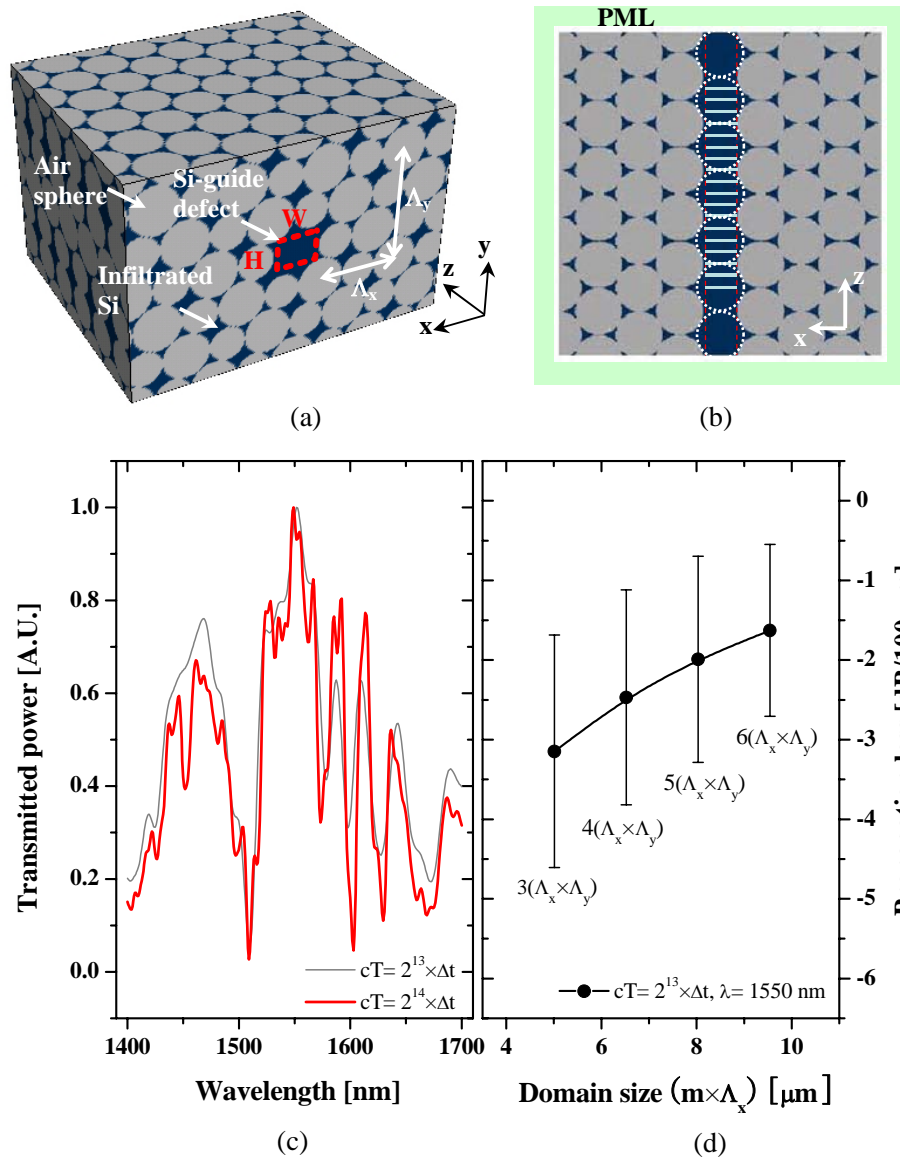


Figure 2.7 (a) Schematic of the self-assembled PC waveguide with a rectangular Si-guide defect ($W/H=0.637\text{-}\mu\text{m}/0.551\text{-}\mu\text{m}$); (b) schematic of computational domain, which PML boundary condition and detection plate are applied; (c) transmitted power spectra detected at $z=10.2\text{ }\mu\text{m}$ as a function of the number of time step (cT): The thin and thick lines show the case of 2^{13} steps and 2^{14} steps, respectively; (d) propagation losses at 1550 nm in wavelength depending on domain size of $m\times(\Delta_x\times\Delta_y)$: A linear fitting was performed on transmitted power data detected along the propagation direction ($z=0\sim 10.2\text{ }\mu\text{m}$). The shown bar represents a fitting error range.

were placed along the propagation direction of z and its cross sectional size was identical with one of the rectangular defect. The detected power was determined by the spatial field distribution localized in at the plates. The perfectly matched layers (PML) shown in Figure 2.7(b) were applied at the boundaries of the PC to absorb any escaped energy and eliminate effectively back reflections. For the spectral characteristic calculation, an impulse excitation was initially applied and discrete Fourier transform of the detected signals was simultaneously performed. A spatial grid size (Δx , Δy , and Δz) of $D/16$ and a temporal step size (Δt) of $D/32$ were employed, satisfying the Courant condition [30], [39]:

$$c\Delta t < \frac{1}{\sqrt{\frac{1}{\Delta x^2} + \frac{1}{\Delta y^2} + \frac{1}{\Delta z^2}}} \quad (2.3),$$

where c is the velocity of light.

Figure 2.7(c) presents the transmitted power spectra detected at $z= 10.2 \mu\text{m}$ depending on the number of computation time step, where a total computation time (cT) in length is represented by the time step number multiplied by Δt . The better spectral resolution is observed at the increased step number of 2^{14} , and enables to inspect the fine peaks in the stopband.

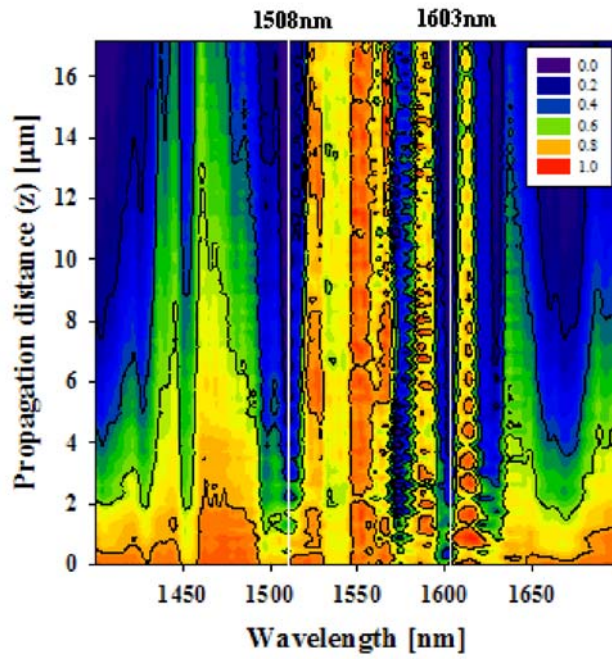
The position of PML may also affect the precision of simulation result, which is directly associated with a computational domain size. The domain size of $m \times (\Lambda_x \times \Lambda_y)$ is defined by Λ_x of $1.507 \mu\text{m}$ and Λ_y of $2.131 \mu\text{m}$, where m is a positive integer, as shown in Figure 2.7(a). As the size becomes smaller, the effect of PBG is much less, and the scattered and escaped signal (even stopband signal) is likely to be directly absorbed at the

PML. Eventually, it will result in degraded spectral characteristics. The effect of the PML position was investigated by calculating the propagation loss variation with the domain size. A linear fitting was performed on the transmitted power data obtained at 1550 nm, where the slope represents the propagation loss. As the domain size is increased by $6(\Lambda_x \times \Lambda_y)$, much enhanced propagation loss is shown in Figure 2.7(d).

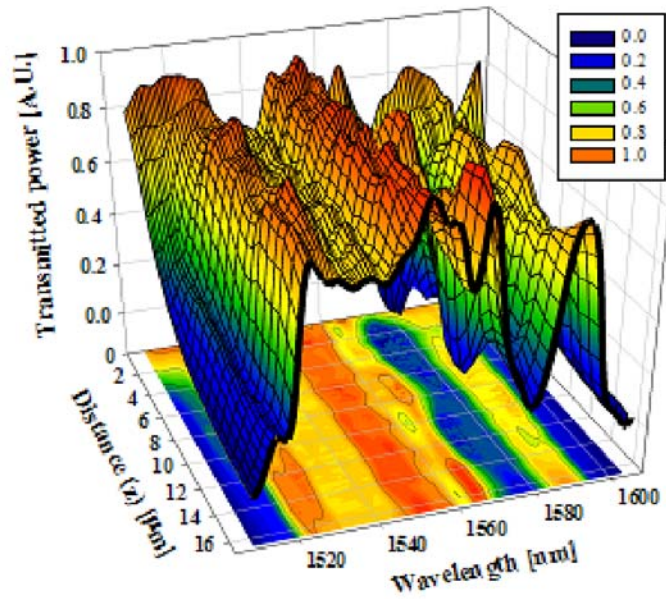
2.4.2 Results & discussion

In this FDTD simulation, the computation step number of 2^{14} and the cross sectional domain of $5(\Lambda_x \times \Lambda_y)$ were used, and the detection plates with spacing of $D/4$ were placed over $z=0 \sim 16.5 \mu\text{m}$. Figure 2.8(a) shows the calculated transmitted power spectra as a function of the propagation distance of z . As the launched light passes thru and interacts with the PC waveguide structure, the powers within the band of 1508~1603 nm (a stopband of the PC) are sustained, but outside this band gradually become evanescent. The band edges with a bandwidth of 6.1 % were defined by the power close to zero, which is comparable to the PBG results obtained by the PWE calculation described in the previous sections. It means that the in-band light signals may propagate through the Si-guide, while out-of-band ones not. Figure 2.8(b) depicts in detail the power spectra within the stopband, and several peaks and dips are observed. The peaks with various magnitudes may be attributed to the existence of defect mode, and the distinctive dips may be local bandgaps formed by the mode interval as reported in [3], [35], [40]-[41].

As a quantitative analysis, a propagation loss calculation in units of dB/100 μm



(a)

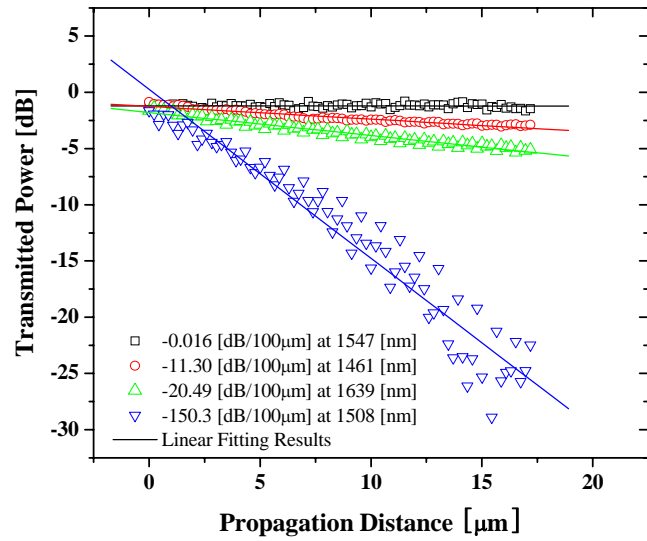


(b)

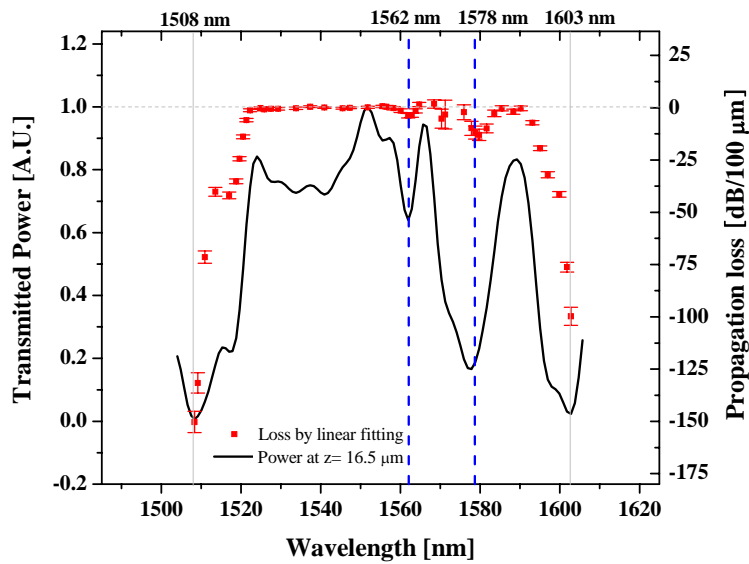
Figure 2.8 Transmitted power spectra depending on propagation distance of $z=0\sim 16.5$ μm : (a) stopband of 1508~ 1603 nm with bandwidth of 6.1 % is defined by two band edges (solid lines) with close to zero-transmitted power; (b) transmitted power spectra within the stopband.

has been performed by the linear fitting method as described in Section 2.4.1. Some selected losses at the inside, outside, and edge of the stopband are shown in Figure 2.9(a). A very small loss of 0.016 dB/ 100 μm was obtained at 1547 nm in the stopband, and high-level losses elsewhere. For a specific inspection of the stopband, two spectra are simultaneously plotted in Figure 2.9(b), where the power spectrum has been detected at $z= 16.5 \mu\text{m}$ as Figure 2.8 (b) and the corresponding propagation loss distribution has been obtained by the same method used in Figure 2.9 (a). Within most of the stopband, low-loss spectral distribution close to the zero-level (dotted line) is obtained except at the dips. Near the band edges, the loss shows a steep increment and eventually reaches up to 100~150 dB/100 μm . It shows that the stopband peaks represent the guided defect modes with low-loss propagation regardless of their own different magnitude of power, which just relies on the spatial power profile monitored at the detection plate. The stopband dips at $\lambda=1562$ and 1578 nm may indicate the local bandgap or the mode crossing as specified in Section 2.3 [40]-[41].

For further studies on the spectral characteristics, the transmitted power spectrum is compared with the band structure of Section 2.3, as shown in Figure 2.10. The a/λ of bandstructure is converted into the corresponding wavelength for a direct comparison with the spectrum. The unique features may be summarized as follows. First, the largest dip near $\lambda= 1578$ nm is originally induced by the local bandgap of $\lambda= 1577\sim 1589$ nm. Moreover, the neighboring surface-like mode of Figure 2.6(b-II) makes its effective width increase, which shows only a very small fraction (or none) of power at the center of defect. The next dip at $\lambda= 1562$ nm is much smaller, and the mode crossing is



(a)



(b)

Figure 2.9 (a) Propagation losses in dB/100 μm at several selected wavelengths of inside (1547 nm), outside (1461 nm and 1639 nm), and edge stopband (1508 nm): They were calculated by linear fitting to the detected powers. The losses range over 0.016~ 150.3 dB/100 μm ; (b) transmitted power spectrum (line) and propagation losses (■ with error bar) in the stopband of 1508~ 1603 nm: The power spectrum was detected at $z=16.5 \mu\text{m}$ and the losses were calculated by the linear fitting. The loss spectrum shows huge extinction ratios at the band edges of 1508 nm and 1603 nm

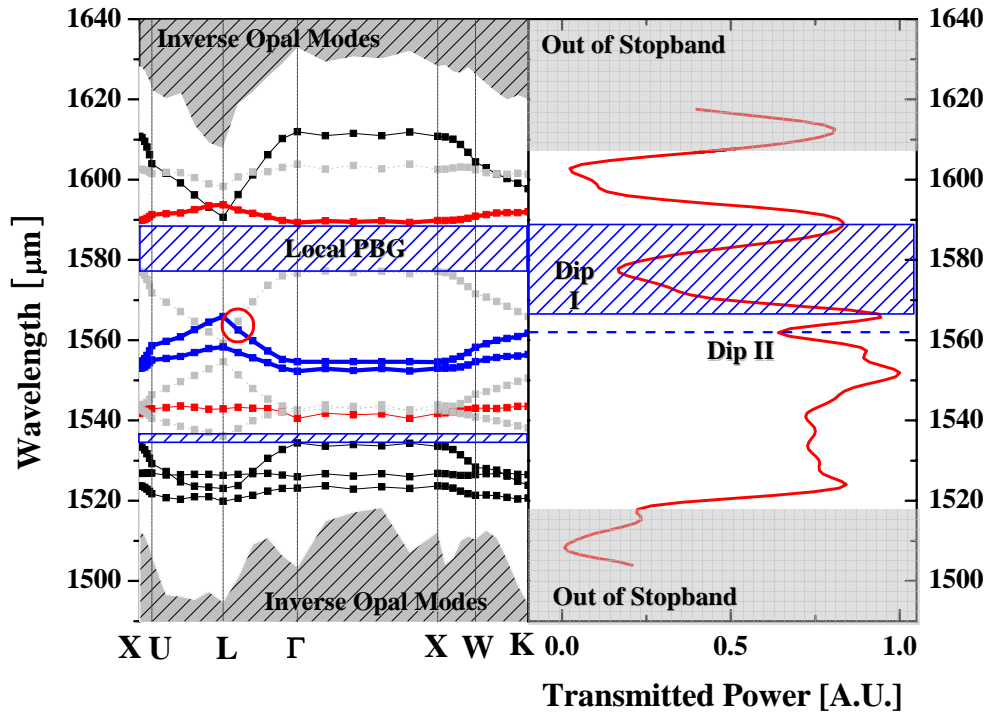


Figure 2.10 Band structure (left) and power spectrum (right) of the inverse opal with a Si-guide defect: The larger dip (Dip I) near $\lambda = 1578$ nm is induced by the local PBG of $\lambda = 1577 \sim 1589$ nm and the surface-like mode of Figure 6(b-II). The smaller dip at $\lambda = 1562$ nm (Dip II) is matched with the mode crossing (circle). The peaks near $\lambda = 1589$ and $1552 \sim 1566$ nm are highly correlated with the guided defect modes of Figure 6(b-I & -III). The peak of $\lambda = 1613$ nm (out-of-stopband) represents an index guided mode. A series of peaks and dips at $\lambda = 1524 \sim 1552$ nm may be due to the dense and complex bandstructure with multiple features (i.e. moderate-intensity fields, mode crossings, and a narrow local bandgap at $\lambda = 1535$ nm). The stopband of $1508 \sim 1603$ nm is comparable with the inverse opal PBG of $1519 \sim 1608$ nm.

observed at the corresponding position of bandstructure, which implies interactions between modes [41]. Second, several distinctive peaks near $\lambda = 1589$ and $1552 \sim 1566$ nm are highly correlated with the guided defect modes with high-intensity field near the

defect center (I and III of Figure 2.6(b)). Third, an isolated and moderate peak of $\lambda=1613$ nm (out-of-stopband) exists but becomes evanescent as shown in Figure 2.8(a), which means an index guided mode. It may initially be confined and guided into the defect due to the higher index of the defect, but gradually it is scattered out of the defect as propagates. Fourth, an obscure zone (a series of peaks and dips) appears at $\lambda=1524\sim 1552$ nm and may be due to the dense and complex bandstructure with multiple features (i.e. moderate-intensity fields, mode crossings, and a narrow local bandgap at $\lambda=1535$ nm). Fifth, the stopband of $1508\sim 1603$ nm is fairly comparable with the inverse opal PBG of $1519\sim 1608$ nm, which obtained by the supercell and PWE method in Section 2.3, as well.

Chapter III: Self-assembled Photonic Crystals

3.1 Introduction

For highly-ordered self-assembled PCs, monodisperse colloidal spheres (such as amorphous silica- or polymer-spheres) are necessary, and various techniques for their preparations have been developed. The well-known chemical synthesis method of silica spherical particles was originally invented by Kolbe and Stöber et al., independently [42]-[43], and further research has continued to improve their quality including monodispersity, size-controllability, spherical morphology and reproducibility, singles purity etc. [44]-[56]. The silica spheres are suitable for post-high-temperature processes due to their better thermal-stability than the polymer ones, and can be much easily employed in the fabrication of inverse opal as a template. At the same time, the self-assembly techniques have also been explored consistently to obtain highly-ordered crystals defining its PBG behavior [9], [57]-[65].

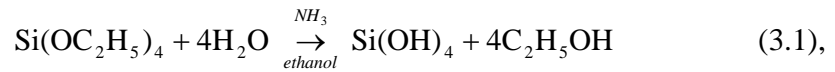
In this chapter, the fabrication of self-assembled opal and inverse opal with a stopband near 1550 nm wavelength is discussed. First, the large monodisperse silica spheres have been prepared by efficient synthesis, preannealing, and centrifuge collection. Through convective self-assembly methods, thin crystalline opal film (only pseudo-PBG) have been built. To achieve complete PBG, additional inverting processes have been performed to the opal (i.e. α -Si infiltration and silica sphere elimination). Eventually, the opal template was successfully transformed into an inverted replica (inverse opal) with

periodically arranged air spheres. Their optical characterization results of SEM inspection and FTIR spectroscopy will also be presented to verify the highly-ordered crystalline structures and stopbands near 1550 nm wavelength.

3.2 High-quality monodisperse silica sphere

3.2.1 Stöber-Fink-Bohn method

Generally, silica spheres have been synthesized by the Stöber-Fink-Bohn method [43], using hydrolysis and condensation of tetraethylorthosilicate (TEOS, $\text{Si}(\text{OC}_2\text{H}_5)_4$) and water (H_2O) in ethanol solutions with a base-catalysis of ammonia (NH_3), as expressed by Equation (3.1) and (3.2) respectively [44].



For the synthesis of silica spheres, two ethanol (99.5 %) solutions of 50 ml with TEOS (≥ 99.0 %, 0.2 M) and NH_3 (NH_4OH of 29 %, 1.8 M) - H_2O (Deionized water of 18.5 $\text{M}\Omega/\text{cm}$, 6.0 M) were initially prepared and quickly combined in a cylindrical reaction vessel with continuous agitation by magnetic stirring. The reaction vessel was placed in a water bath of 20.0 °C to maintain constant reaction temperature.

The reaction was usually continued for about 4 hours, expected to be long enough to complete the reaction. Figure 3.1 shows the size of synthesized spheres as a function of

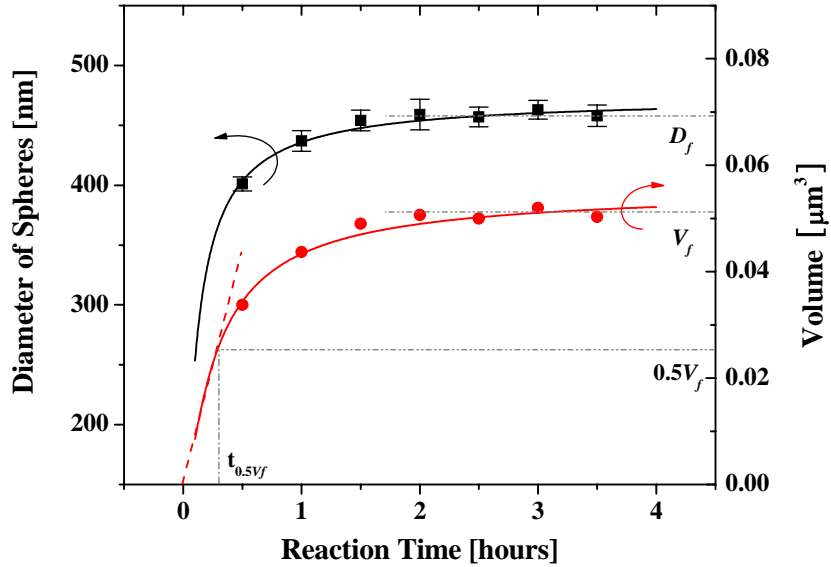


Figure 3.1 Measured diameters and calculated volumes of silica sphere synthesized by the Stöber-Fink-Bohn method as a function of reaction time: A steep growth rate is shown till the $t_{0.5V_f}$ of 17.5-min, where $t_{0.5V_f}$ is the time to be half of final volume ($0.5V_f$). The sphere of $0.5V_f$ is produced by consuming half of TEOS ($0.5k_0$), where k_0 is the total initial TEOS amount. After the reaction completion, the spheres of $D_f= 458 \text{ nm} \pm 2.0 \%$ and $V_f= 0.050 \mu\text{m}^3$ were obtained.

reaction time. Each average diameter (D) and standard deviation (σ) was measured over 50~100 spheres using the images of JEOL JSM 6500 Field-Emission Gun Scanning Electron Microscope (FEGSEM). The sphere volume (V) was calculated by the diameter to investigate its growth rate. The growth profile initially shows a steep increase to half of final volume ($0.5V_f$), and then gradually decreases and reaches its final volume (V_f), as shown in Figure 3.1. As the sphere gets larger and its surface area (reaction area) increases, TEOS is rapidly consumed and the growth eventually stops. After the TEOS

was completely consumed (about 4 hours), the obtained spheres ($D_f = 458 \text{ nm} \pm 2.0 \%$ and $V = 0.050 \text{ } \mu\text{m}^3$) were washed with deionized water and/or pure ethanol through several cycles of centrifugal sedimentations and sonications to remove the remaining impurities such as NH_3 , H_2O , and TEOS [45]. Using this procedure, a colloidal silica sphere suspension with a certain desired concentration in ethanol may be prepared.

For the self-assembled opals and inverse opals with a stopband near 1550 nm wavelength, the large and monodisperse silica spheres of approximately 710 nm and 870 nm diameters are required, respectively. They may be grown by controlling various synthesis conditions such as concentration of reactants, reaction temperature, and the kind of solvent, etc. [44]-[45]. It was however not easy to produce the high-quality large monosized spheres by the one-step method because of poor monodispersity and reproducibility resulting from possible variations of the process conditions.

3.2.2 Seeded growth technique

A seeded growth technique with much better size control has been utilized to synthesize the monodisperse and large silica spheres [47]-[51]. Regardless of the seed size, it is possible to adjust the final sphere to the required size by repetitive extra TEOS additions into the seed suspension prepared by the Stöber-Fink-Bohn method. The TEOS is periodically added at specific intervals (t_s) defined by complete TEOS consumption. Each extra growth also follows an equivalent profile to the seed's. Figure 3.2 shows the stepwise growth profile in volume depending on the additions. The total addition amount

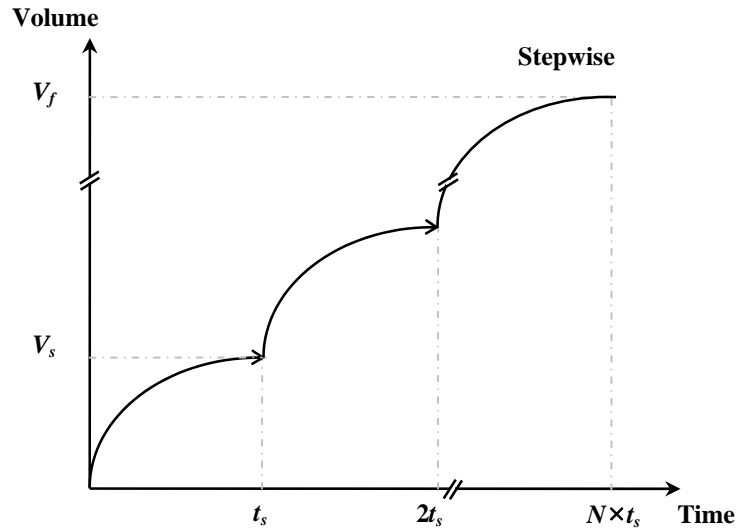


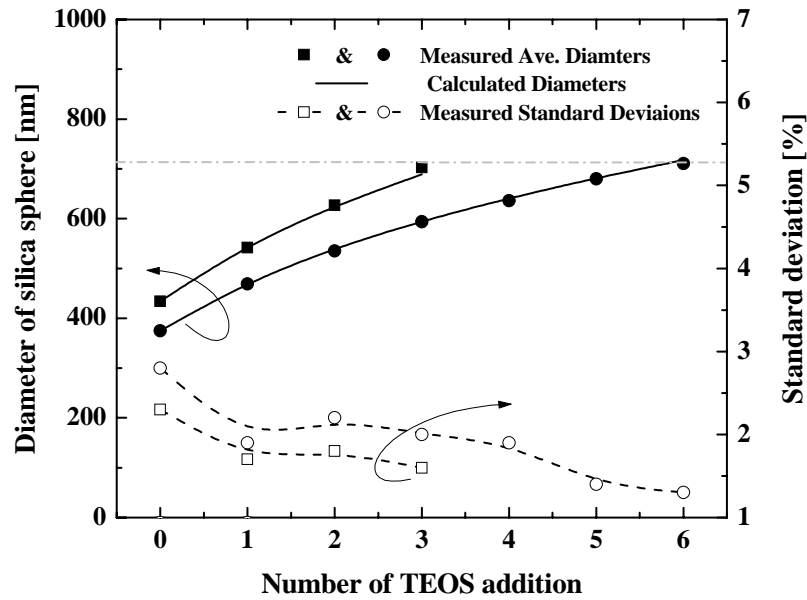
Figure 3.2 Schematic growth profile of silica spheres (stepwise) in seeded growth technique: t_s is addition interval, N is the number of additions, and V_s and V_f are seed and final sphere size in volume, respectively.

of TEOS (k_s) may be estimated by the required final diameter (D_f) or volume (V_f), the seed diameter (D_s) or volume (V_s), and the amount of TEOS (k_0) used in initial seed synthesis [49]:

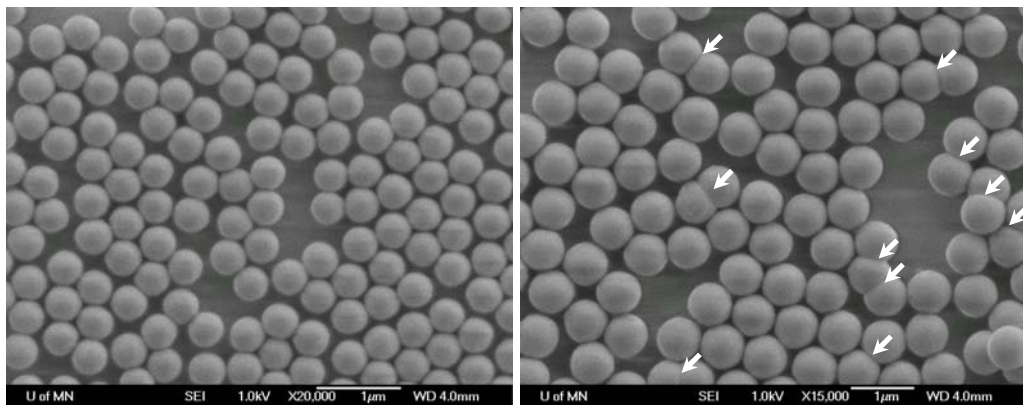
$$\frac{D_f}{D_s} = \sqrt[3]{\frac{V_f}{V_s}} = \sqrt[3]{1 + \frac{k_s}{k_0}} \quad (3.3),$$

where k_s/k_0 represents the total number of TEOS addition (N).

The silica spheres with the required D_f of 710 nm could eventually be obtained using this seeded growth technique, as shown in Figure 3.3(a). Initially, two seed suspensions with 434 nm and 375 nm diameters were separately prepared under the same reaction conditions as described in Section 3.2.1. The extra TEOS was subsequently and



(a)



(b)

(c)

Figure 3.3 (a) Diameters and standard deviations of silica spheres obtained by seeding growth technique: After 3 and 6 TEOS additions, the seeds of $D_s = 434$ nm \pm 2.3 % and 375 nm \pm 2.8% were grown up to $D_f = 703$ nm \pm 1.6% and 711 nm \pm 1.3%, respectively; SEM images: (b) seed spheres by Stöber-Fink-Bohn method ($D_s = 434$ nm); (c) synthesized spheres by seeded growth technique ($D_f = 703$ nm): The arrows denote the aggregates with spheres.

quickly introduced at about 4-hour intervals into the suspension itself, where only TEOS was completely consumed, but H₂O and NH₃ still remain. Although the H₂O and NH₃ are consumed or evaporate in the middle of reaction, no critical effect has been observed in these experiments. The practical TEOS amount of being equal or less than k_0 was selected by the k_s of Equation (3.3) to prevent small particles (nuclei) created by secondary nucleation [50]. The nuclei can be effectively removed in the middle of the washing process, but its formation represents a loss of TEOS and may lead to reduce the actual D_f . By the three and six TEOS additions, larger spheres of 703 nm and 711 nm diameters with narrow standard deviations (1.6% and 1.3%) were eventually obtained, respectively. As the TEOS additions proceeded, the standard deviations (monodispersity) were reduced. The measured mean diameters depending on the addition number were in good agreement with ones calculated by Equation (3.3).

However, a large amount of aggregates with spheres (such as doublet, triplet, and others) were observed in the colloidal suspensions, as shown in Figure 3.3(c). The aggregates may become critical defects to disturb the opal formation. In the following Section 3.2.3, the various methods to improve the purity of singles will be discussed.

3.2.3 Preparing monodisperse single-spheres

To prepare monodisperse single silica spheres suppressing the undesired aggregates, two experiments were independently performed. A slow agitation (magnetic stirring) was first applied to reduce collision opportunity between silica spheres in the

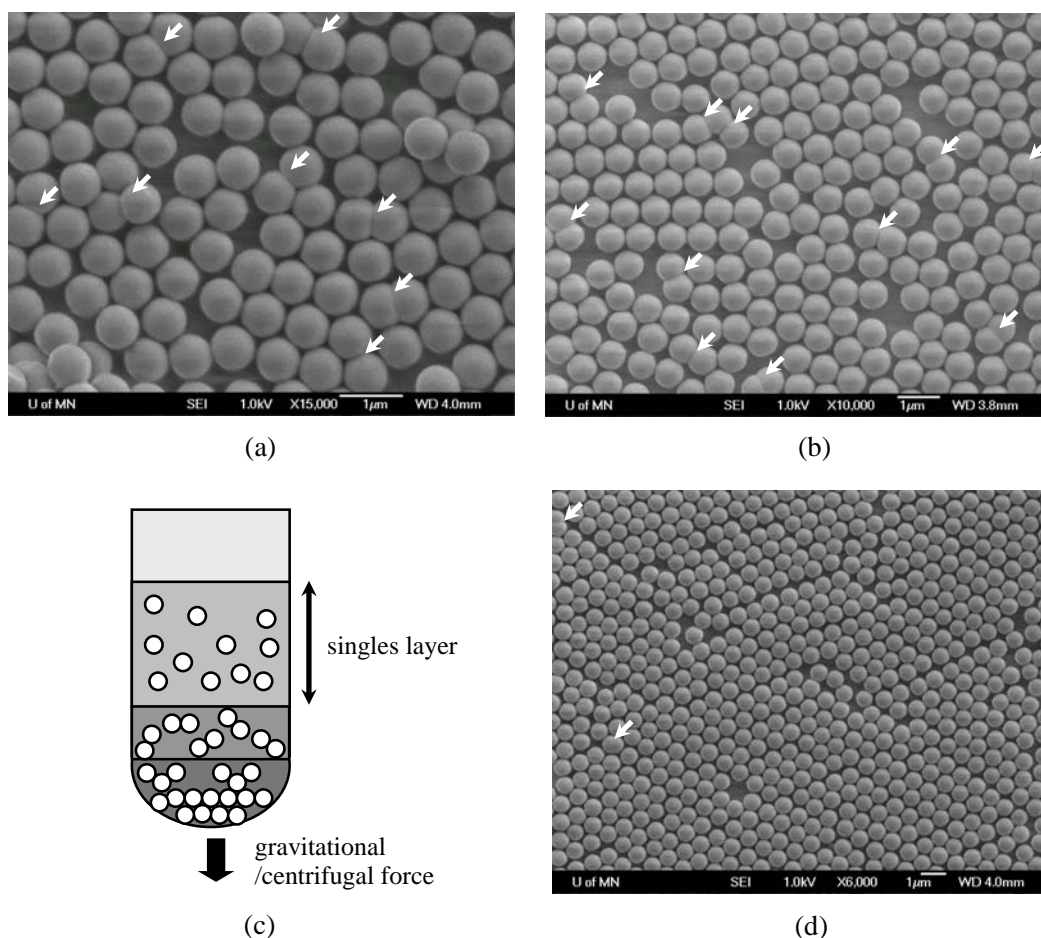


Figure 3.4 SEM images of silica spheres containing (a) 8.8 % and (b) 3.0 % aggregates (white arrows), synthesized with 900 rpm and 300 rpm magnetic agitations, respectively; (c) schematic diagram of singles collection technique by sedimentation of the aggregates; (d) SEM image of 0.3 % aggregates after centrifuge collection (1000 rpm, 13-min).

middle of the synthesis. In the previous synthesis with an agitation speed of 900 rpm, 8.8 % aggregates (most of doublets) were observed in the SEM images, which were inspected over 1000 spheres, as shown in Figure 3.3(c) and 3.4(a). On the other hand, at the much lower speed of 300 rpm, much reduced aggregates of about 3.0 % could be obtained, as shown in Figure 3.4(b).

Next, for the much purer colloidal suspensions of singles, a collection technique using the centrifuge was employed. A separation method using sedimentation suggested by P. Ni et al. [52] makes the silica spheres settle down in the suspensions by the gravitational force. As it progresses, an isolated layer of singles distinctively appears due to sedimentation velocity differences between singles and other aggregates, as shown in Figure 3.4(c). Although the singles are separated and collected from the undesired aggregation, it is a time-consuming process due to the long sedimentation time. Alternatively, centrifugal force was able to accelerate the process. Relative centrifugal force of $146\times g$ associated with a rotating speed of 1000 rpm and a centrifuge radius of 13.1 cm was gradually applied within the suspension of about $10\text{ wt}\%$ for about 13 mins . After the centrifugation, only small amount of suspension (about 3 ml at a time) was carefully collected with a thin pipette or a syringe. Through the singles collection, a much purer colloidal suspension with only 0.3% aggregates was prepared, as shown in Figure 3.4(d). The technique with much reduced process time may simply be repeated to acquire enough purity.

3.2.4 Efficient fast growth method

In the previous seeded growth technique, the long reaction time (about 16~ 28 hours) has been required and even more time has been reported [45], [47]. It may be inefficient in the larger sphere synthesis, and moreover the undesired aggregates may occur by the increased collision opportunity of spheres. The reaction time effect on the aggregates can be found in the comparison of seed and final spheres, as shown in Figure

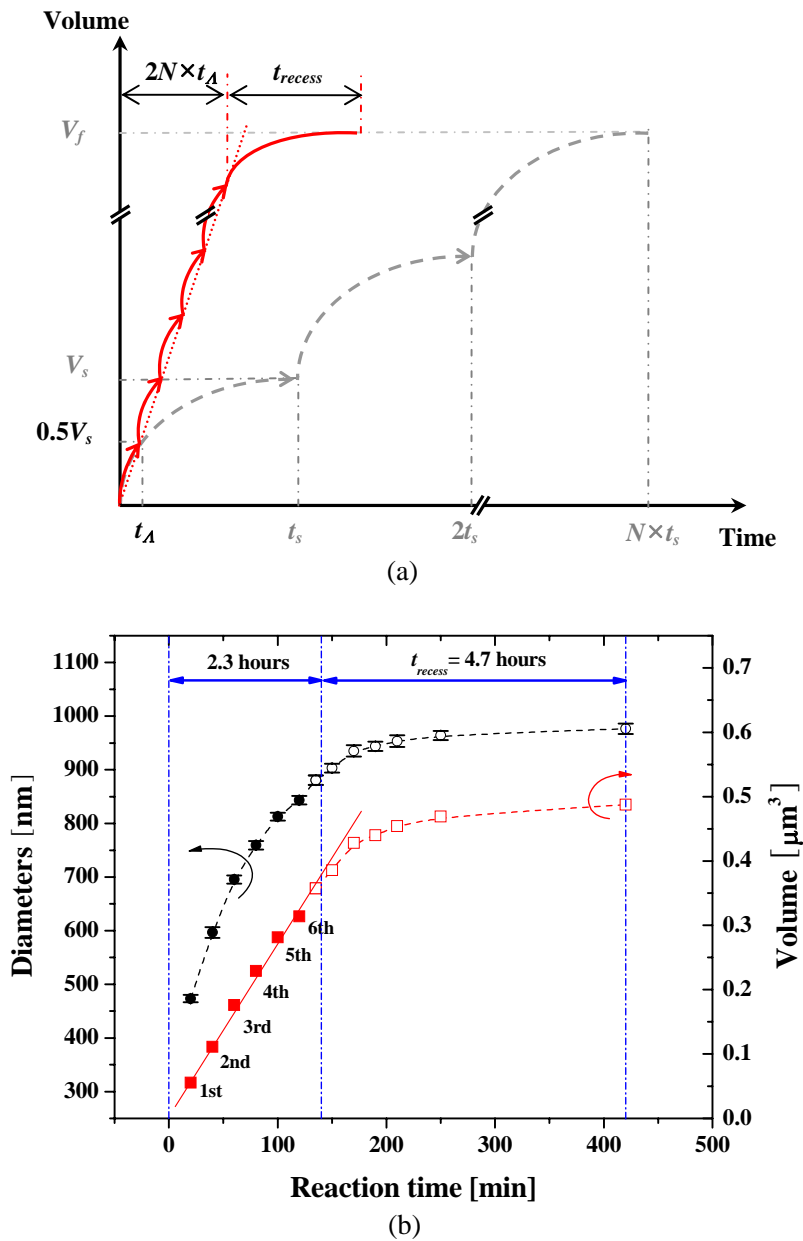


Figure 3.5 Schematic (a) and actual growth profiles (b) of the modified seeded method and the conventional one: The modified method has a faster growth profile (during the addition period of $2N \times t_A$) through a short interval of t_A (20-min) and a reduced addition amount of $0.5k_0$. The spheres with $D_f = 977 \text{ nm} \pm 1.0 \%$ and $V = 0.487 \mu\text{m}^3$ were obtained after total 7-hour reaction.

3.3(b) and (c). The growth method has therefore been modified to have an effectively reduced reaction time by utilizing the initial steep growth, mentioned in Section 3.2.1. It has been simply accomplished by only adjusting the TEOS addition amount and interval without any change of reagent or facility. The new interval (t_A) was chosen by a time ($t_{0.5V_f}$) required to be grown up to half of final volume ($0.5V_f$), as depicted in Figure 3.1. In other words, it is an equivalent time to consume half of total TEOS ($0.5k_0$) with the steep growth. By refilling the consumed amount for the interval of t_A , the steep region may continuously be extended, as shown in Figure 3.5(a). The reaction time and the number of aggregates may be much reduced than the conventional one even though twice N is required.

In the practical experiment, the t_A of about 20 min (slightly more than $t_{0.5V_f}$) and the addition amount of slightly less than $0.5k_0$ were applied in order to suppress nuclei formations. During the addition period ($2N \times t_A$ of 2.3 hours), six additions were carried out by quick injection into the reactants which was continuously agitated with a speed of about 600 rpm. Subsequently, a recess time (4.7 hours) was given to complete the final progressive growth. The produced spheres during the $2N \times t_A$ have been enlarged following the linearly steep growth profile, as represented in Figure 3.5(b). For a precise adjustment to D_f , an exact final addition amount has simply been estimated through the SEM characterization and Equation (3.3) before the last addition step. After total 7-hour reaction, the monosized large silica spheres ($D_f = 977 \text{ nm} \pm 1.0 \%$ and $V_f = 0.487 \mu\text{m}^3$) were produced rapidly.

The prepared colloidal spheres have subsequently been washed and inspected over 1000 spheres in SEM images. Figure 3.6 is two of the selected SEM images used in the inspections, which contains silica spheres ($D_f = 910 \text{ nm} \pm 1.6 \%$ and $V_f = 0.395 \mu\text{m}^3$) grown by the effective method. The aggregates of only 0.6 % were counted, and there was only a small chance to find the nuclei due to being removed in the middle of the washing process as mentioned earlier. The suppressed amount of aggregates are much less than the conventional seeded growth product and comparable with the collected ones by the centrifuge, as described in Section 3.2.3.

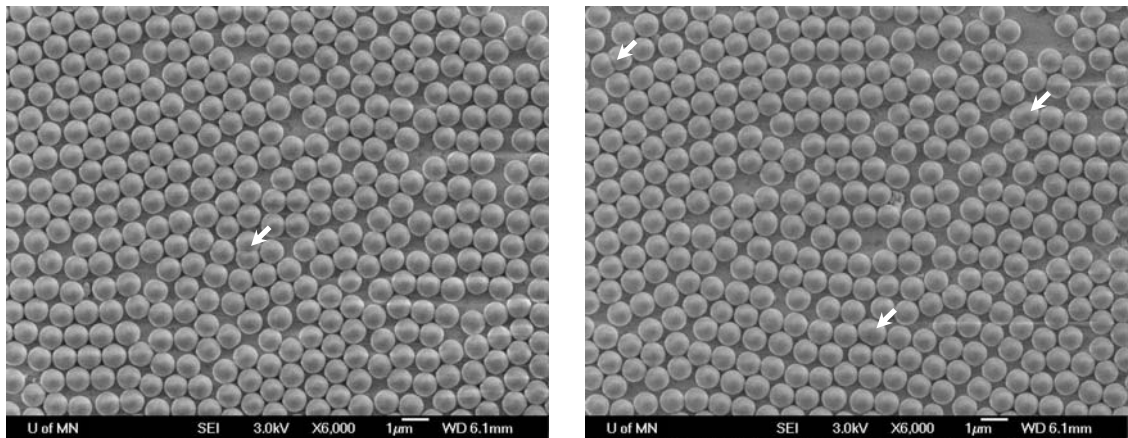
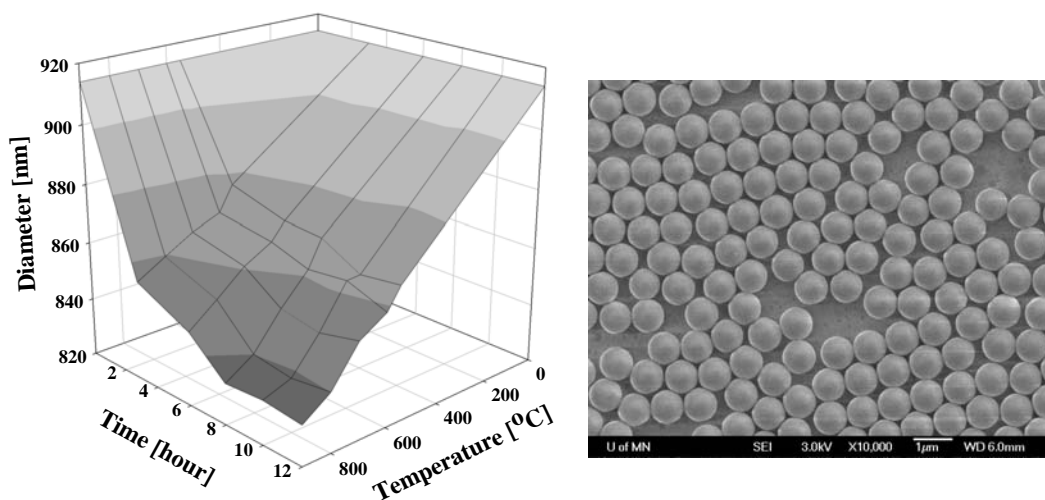


Figure 3.6 SEM image of silica spheres ($D_f = 910 \text{ nm} \pm 1.6 \%$ and $V_f = 0.395 \mu\text{m}^3$) containing aggregates of 0.6 % (white arrows, inspected over 1000 spheres).

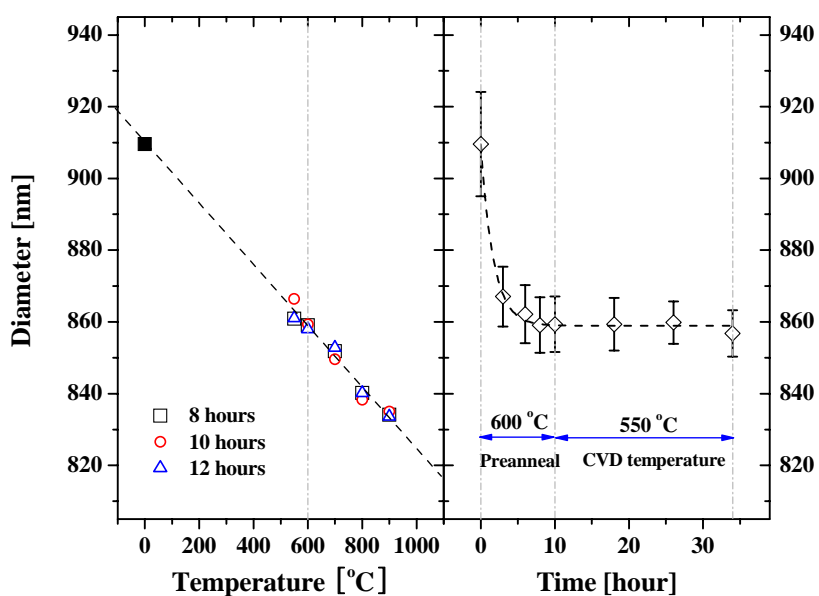
3.2.5 Shrink-proof spheres

For infiltrating amorphous silicon ($\alpha\text{-Si}$) into the silica opal template, a low-pressure chemical vapor deposition (LPCVD) process has been widely used [9].



(a)

(b)



(c)

(d)

Figure 3.7 Thermal shrinkage of silica spheres ($D=910\text{ nm} \pm 1.6\%$): (a) overall profile under $550\sim 900\text{ }^\circ\text{C}$ for $3\sim 12\text{-hour}$; (b) SEM image of the preshrunk spheres ($600\text{ }^\circ\text{C}$ for 10 hours , $D=859\text{ nm} \pm 0.9\%$); (c) saturated sizes after $8\sim 12\text{-hour}$ preannealing and linear size variations depending on the annealing temperature; (d) size variation under $550\text{ }^\circ\text{C}$ for 24-hour (equivalent to CVD conditions) after $600\text{ }^\circ\text{C}$ preannealing for 10-hour : Any deformation of silica spheres has not been observed under the investigated annealing conditions.

However, this leads to a volumetric shrinkage of silica spheres [54]-[56] because of the high deposition temperature (near 550 °C), and serious cracks reducing the grain domain size may occur in the inverse opal. The structural defects have considerably been overcome by annealing the spheres at the temperature in advance, as suggested by [56]. The slightly larger size than the theoretical one ($D= 870$ nm) have eventually been required taking account of the thermal shrinkage rate.

A shrinkage profile on the previously prepared silica spheres ($D= 910$ nm \pm 1.6 %) has first been investigated under the various annealing temperatures and duration times (550~ 900 °C, 3~ 12 hours), as in Figure 3.7(a). The thermal treatment has been performed in air atmosphere with a ramp rate of 5 °C/min and natural cooling. The upper and lower temperature limits were chosen for a deformation-free temperature and a practical CVD temperature, respectively. No deformation of the preshrunk silica spheres has been observed under the investigated conditions as presented in Figure 3.7(b). In this experiment, two of distinctive features have overall been observed. First, as increasing the annealing time under a fixed temperature, the sizes have been gradually saturated passing through an initial rapid shrinkage period. After 8~ 12-hour annealing, the size shrinkages have nearly been stopped at the investigated thermal conditions, as shown in Figure 3.7(c). The next is linear size-variations depending on the annealing temperature. It is different with the gradual size-saturation reported by [56], and the deviation might be induced by the different reaction conditions (or method) used in the silica sphere growth. The linear variation feature is also clearly presented in Figure 3.7(c).

Based on the profile, the actual preannealing conditions (600 °C and 10-hour) have been properly determined and utilized to prepare shrink-proof silica spheres. To confirm the shrink-proofing, the preshrunk spheres have been reheated at the CVD temperature (550 °C) for 24 hours, as in Figure 3.7(d). It shows quite small size-variation near 859 nm diameter after the preannealing, and may verify the thermally treated silica spheres in advance would not shrink further in the middle of the CVD process. Moreover, enhanced monodispersity (σ of less than 1.0 %) has been observed in the shrink-proof spheres of Figure 3.7(d).

3.3 Self-assembly & inverting processes

To build the opal with large domain size, various self-assembly techniques have been studied and developed for the past decade, such as sedimentation, spin-coating, repulsive electrostatic interaction, and capillary meniscus method, etc. The capillary meniscus (also known as vertical deposition method by Colvin et al. [57]) is feasible to build a thin opal film and suitable for the compact integrated applications. It can be formed on a vertically submerged substrate into the suspension, which has a controlled concentration of spheres in an alcoholic solution, as depicted in Figure 3.8(a). Using natural evaporation, the meniscus is gradually pulled down along the substrate, where the self-assembly occurs. The opal thickness from one to tens of layers may be controlled by varying the sphere concentrations. This method is however not suitable for large silica spheres (diameters of more than 500 nm) because of its natural sedimentation.

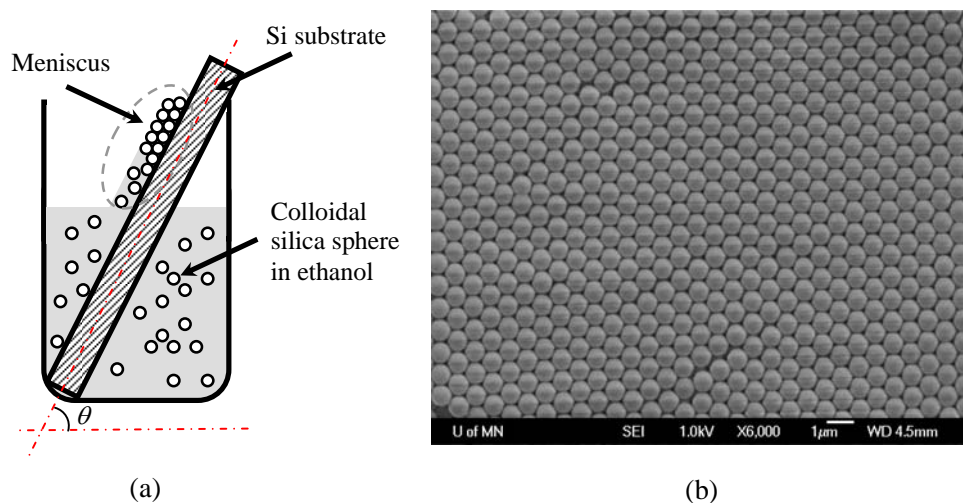


Figure 3.8 (a) Schematic setup diagram of convective capillary meniscus method; (b) SEM top-view image of opals, where silica spheres ($D_f= 703$ nm) form a closed-packed periodic structure.

3.3.1 Convective self-assembly method

In self-assembly of 703 nm diameter spheres prepared in Section 3.2.2., a convective self-assembly method has been used [9], which is a heat-assisted meniscus method. Thermal gradient applied in the colloidal suspension leads to its convection and restrains the gravitational sedimentation of spheres by the convection. It eventually enables the large spheres to be continuously supplied to the meniscus and even reduces its process time through the increased evaporation rate. The experimental setup was designed to have about 10 °C temperature difference between the top and bottom of vial as it was embedded into the thermostatically controlled sand bath. An enclosure may be used to maintain constant solvent evaporation and protect possible random airflow.

Two critical self-assembly conditions, evaporation temperature and slope angle (θ) of the submerged substrate, have precisely been studied to build uniform opalescent structure. Figure 3.8(b) presents the opal structure produced on a declined Si-substrate ($\theta=60^\circ$) and at 60 °C. The temperature was monitored in the atmosphere within the enclosure. The colloidal suspension containing 1 wt% spheres was prepared with pure ethanol solution. The opal film was uniformly covered over $1\times 3\text{ cm}^2$ without any critical longitudinal and/or lateral discontinuity, although it had grain domain sizes of several tens micrometers limited by natural cracks. A self-assembly result with similar conditions (except temperature) has also been reported by López et al. [60].

However, the convective method has not been suitable for much larger and heavier spheres (above 800 nm diameters after the preannealing process) and it was difficult to obtain such a uniform opal film over the large area because of a discontinuous self-assembly induced by insufficient sphere-transfers to the meniscus.

3.3.2 Assisted convective-method by the Marangoni effect

For the larger and heavier sphere deposition, a modified convective method using an aqueous binary mixture (water & 1-propanol) instead of the pure alcoholic solution has been developed by Jun [61]. A continuous transfer for the large and heavy spheres to the capillary meniscus is feasible to be accomplished by the Marangoni effect [61], which is a mass-transfer (fluidic flow) from low- to high-surface tension region caused by concentration and/or temperature gradient. For example, a fluidic motion (like tears of

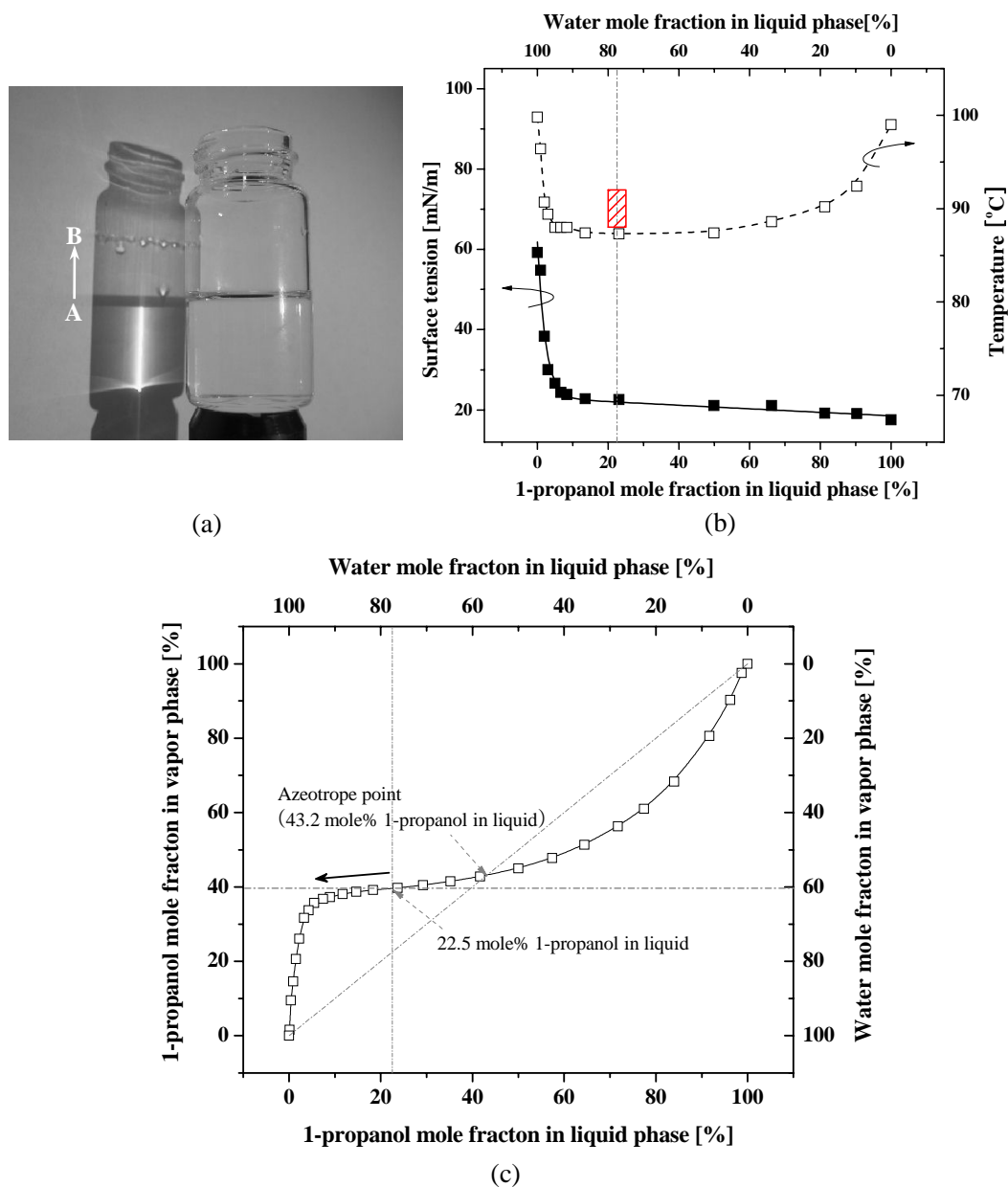


Figure 3.9 (a) Marangoni effect in the aqueous 1-propanol (9.1 mol%, at ambient temperature of 20 °C) mixture. The fluidic flow (from A to B) at the meniscus is induced by concentration gradient; (b) surface tensions and boiling points of the mixture depending on compositions in liquid phase [64]-[65]: A hatched area shows the available self-assembly conditions (88~ 92 °C and 20~ 25 mol% 1-propanol in liquid phase) proposed by Jun [62]; (c) phase diagram of the mixture at 100 MPa [63].

wine) can be easily observed on a container sidewall filled with the mixture, as shown in Figure 3.9(a) where the aqueous mixture was prepared with 1-propanol of 9.1 mol% at 20 °C. As naturally evaporated, the compositions at the original mixture (level A: higher concentration of 1-propanol) and the meniscus (level B: lower concentration of 1-propanol) result in nonequilibrium, and a concentration gradient is built on the sidewall. The fluid can eventually flow up from A (low surface tension) to B (high surface tension), and then the formed droplets at the B naturally fall back down.

Figure 3.9(b) shows the surface tensions and boiling points of the mixture depending on the compositions in liquid phase [62]-[65]. The suggested self-assembly conditions (88~ 92 °C and 20~ 25 mol% 1-propanol in liquid phase) in [62] are also depicted as a hatched box, where much stable surface tension and boiling point are provided over the composition range (even larger). Although the initial composition is placed at the deviated azeotrope point (left part) and the liquid becomes evaporated (solid arrow) as shown in Figure 3.9(c) [63], the composition in liquid and vapor phase can be nearly constant over a large range. The continuous sphere-transfer may be maintained by the built-in concentration gradient during the self-assembly.

In the practical self-assembly, a colloidal suspension containing about 10 wt% silica spheres in the aqueous 1-propanol (23.1 mol%) mixture has initially been prepared in a vial. The shrink-proof silica spheres ($D = 853 \text{ nm} \pm 1.0 \%$) were employed after collecting singles by the centrifuge, as described in Section 3.2.3, and there was very little chance to detect the aggregates by the SEM image inspection. The identical experimental set-up described in Section 3.3.1 has been used, and a Si-substrate was

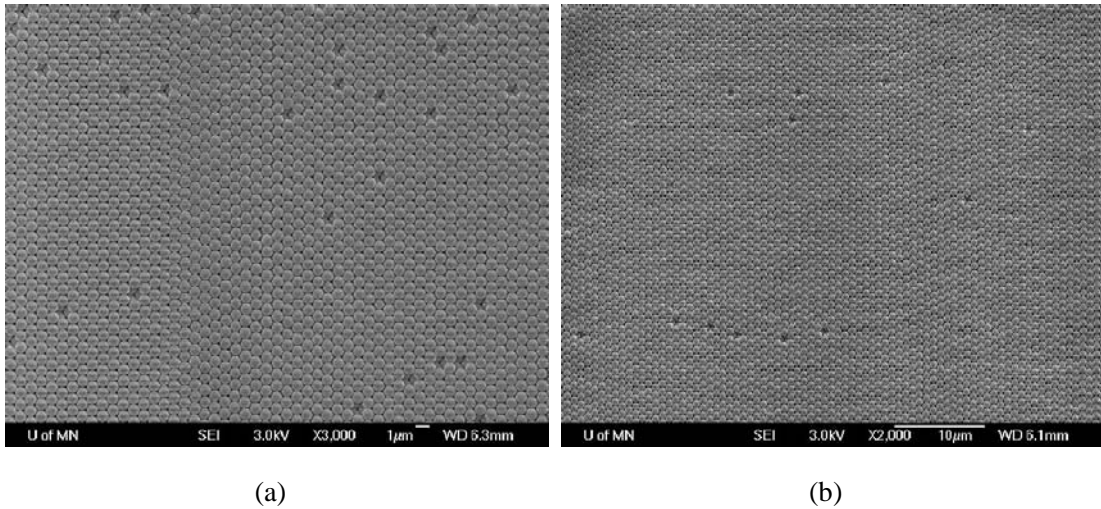


Figure 3.10 SEM top-view images of self-assembled opal with different magnifications ((a) $\times 3000$, (b) $\times 2000$): The opal was deposited by the convective method using aqueous 1-propanol mixture of 23.1 mol%. The grain domains of about $100 \mu\text{m}^2$ and some sphere vacancies have been observed. The vacancies are distributed only on the opal surface.

almost vertically placed ($\theta = 80^\circ$) into the colloidal suspension. The thermal energy applied in the sand bath has been automatically controlled to maintain the mixture evaporation temperatures of $88\sim 92^\circ\text{C}$. Figure 3.10 shows SEM top-view image of the produced opal film whose grain domain size was much larger (about $100 \mu\text{m}^2$) than the previous ones. Some sphere-vacancies distributed only on the opal surface have been observed, but the point defects may not be critical to the embedded waveguide application.

3.3.3 Amorphous silicon (α -Si) inverse opals

An infiltration of a high-index material (more than 2.85) into the interstitial space of opal is necessary to build the inverse opal with complete PBG, as in Figure 3.11(a).

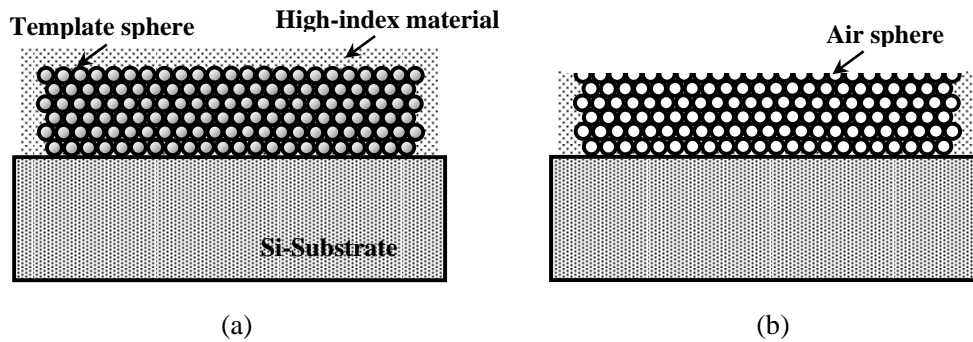


Figure 3.11 Schematics of opal inverting processes: (a) infiltration of high-index material into the opal template; (b) inverse opal with air spheres after some selective etching processes.

Recently, the various infiltrations of some candidate materials have been demonstrated [8], [67]-[71]. For the Si-material, low-pressure chemical vapor deposition (LPCVD) compatible with the CMOS fabrication technology has also been utilized successfully [9]. The low-temperature of deposition (near 550 °C, α -Si) made it possible for homogeneous and complete infiltration while avoiding internal surface roughness. After the filling step, the template spheres can be eliminated by an etching processes to create air spheres. The schematic of Figure 3.11(b) represents the inverse opal comprising the air spheres.

First, for the α -Si infiltration, the low-temperature LPCVD has been performed with a pure silane (SiH_4 , 90 sccm) gas. During the deposition time of about 4 hours, the tube temperature and pressure was constantly maintained at 550 °C and 750 mTorr. Subsequently, the α -Si film over-grown on the top surface was removed by a reactive ion etching (RIE), where the gases of SF_6 (12 sccm), O_2 (2 sccm) and Ar (5 sccm) were used at chamber pressure of 40 mTorr and RF power (20 W), and a high enough etching

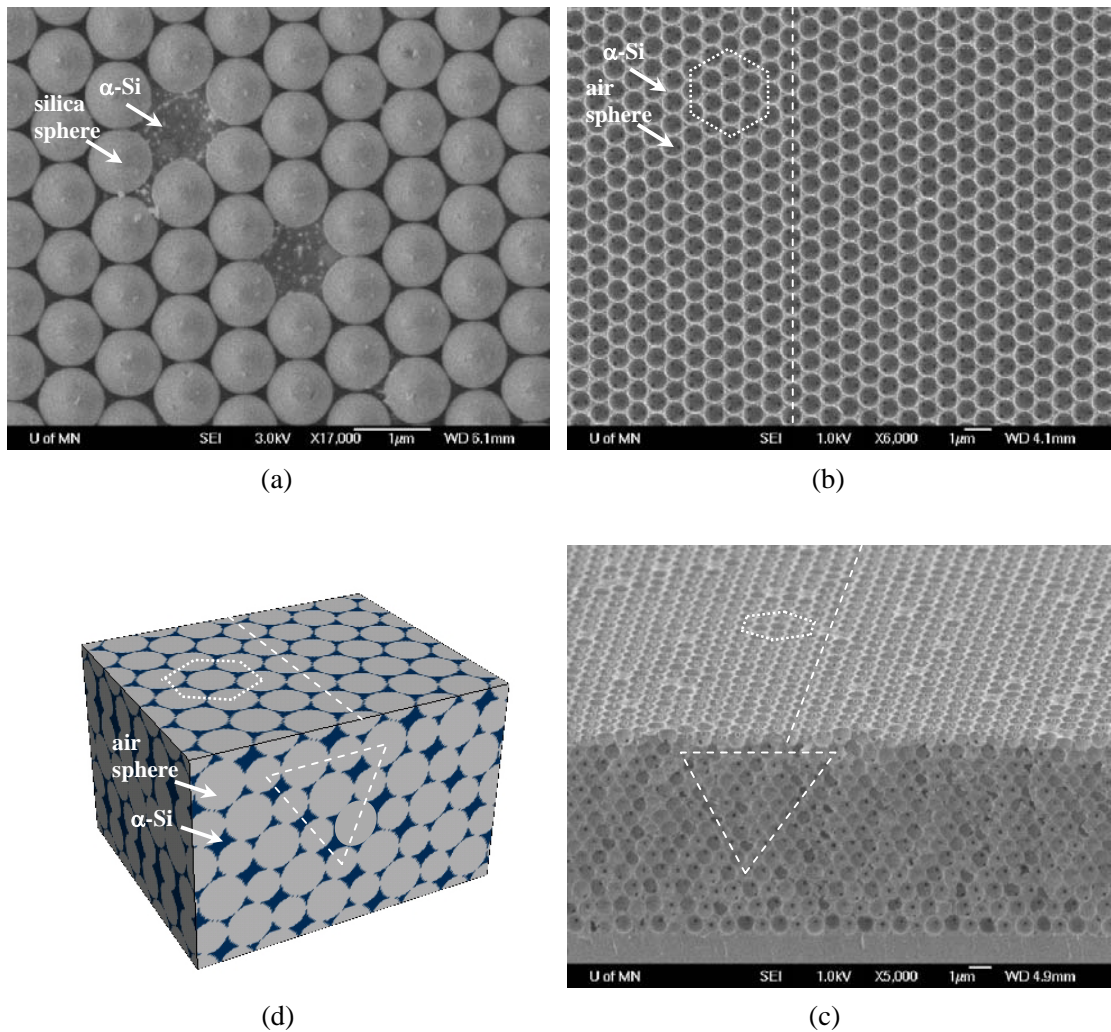


Figure 3.12 SEM images of self-assembled inverse opals with *fcc* closed-packed structure: (a) top-view of the α -Si infiltrated opals after RIE to remove top α -Si layer and expose silica spheres; (b) top-view after removing silica spheres; (c) cross-sectional view; (d) schematic *fcc* closed-packed structure. The dotted and dashed reference lines represent the produced inverse opal has an ideal *fcc* closed-packed arrangement.

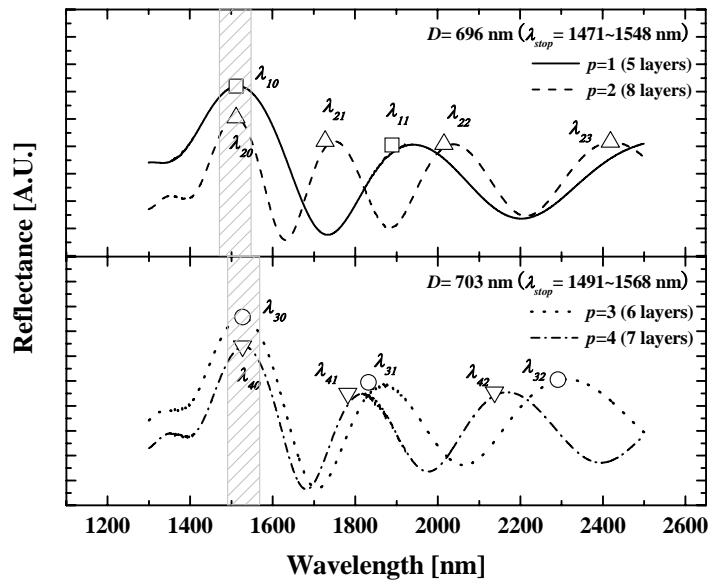
selectivity (α -Si: α -SiO₂) was provided. The exposed silica spheres are observed at the top-surface (embossed) view of Figure 3.12(a).

Through the exposed top spheres and their tiny holes created at the contact point between spheres, the entire spheres could be selectively etched by the penetrated aqueous hydrofluoric acid (HF, 25:1). The fabricated α -Si inverse opal structure was inspected in detail by SEM, and the top and cross-sectional views are shown in Figure 3.12(b) and (c). The images were also compared with an ideal schematic structure (Figure 3.12(d)) using some reference lines traced on the top and cross-section surfaces, and an ideal *fcc* closed-packed arrangement was confirmed.

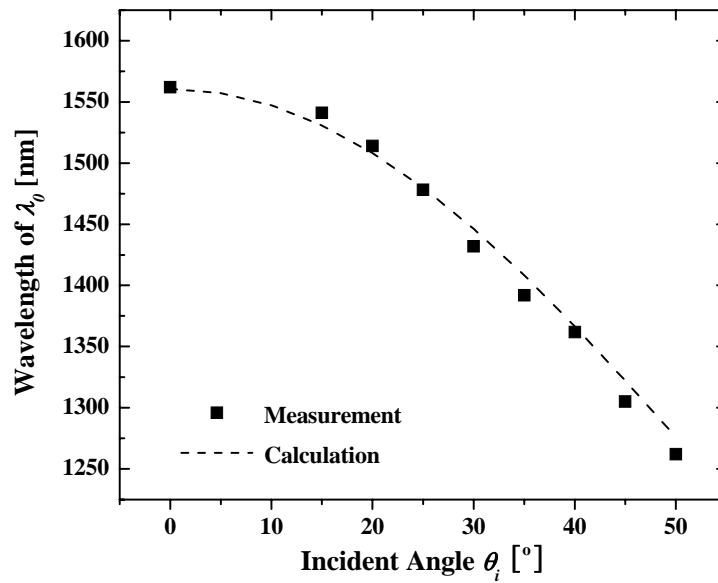
3.4 Characterizations by Fourier transform infrared (FTIR) spectroscopy

As an optical characterization of the self-assembled PCs, some reflectance spectra have been measured to explore its stopband behavior as well as properties of crystalline structure. A Fourier transform infrared (FTIR) spectrometer (Nicolet Magna 750) has been utilized, which is equipped with a MCTA detector, a KBr beam splitter, a variable angle specular reflectance accessory, and a white light source.

The normal-incident reflectance was first measured on the opal surface. Figure 3.13(a) represents the resulting spectra depending on the opal layer number ($N_{layer}= 5\sim 8$). The specimens had been prepared by the self-assembly of 696 nm or 703 nm diameter spheres. Each stopband (λ_{stop} , hatches) corresponding to a pseudo-PBG ($a/\lambda= 0.636\sim 0.667$) is exactly placed on the main peak, where the pseudo-PBG had been obtained in the calculated bandstructure of Section 2.2.



(a)



(b)

Figure 3.13 FTIR spectroscopy results of opals: (a) normal-incident reflectance spectra depending on opal layer number: The theoretical stopbands (λ_{stop} , hatches) are placed at the main peaks. Open symbols are theoretical positions of zero-order main peaks (λ_{p0}) and q^{th} -order sub-peaks (λ_{pq}), where p represents the sample number; (b) experimental and theoretical λ_0 at various oblique incident angles.

The main- and sub-peak spectral positions were also verified clearly by the following Equation (3.4) and (3.5). First, the zero-order main peak position (λ_0) were calculated by the combined Bragg's and Snell's laws [72], as in

$$\lambda_0 = \frac{2d_{hkl}}{m_B} \sqrt{n_{eff}^2 - n_{air}^2 \sin^2 \theta_i} = \frac{2}{m_B} \left(\sqrt{\frac{2}{3}} D \right) \sqrt{n_{eff}^2 - n_{air}^2 \sin^2 \theta_i} \quad (3.4),$$

where d_{hkl} is the inter-planar spacing in the [111] crystalline direction, D is the sphere diameter (obtained by SEM characterization), n_{eff} is the effective refractive index, m_B is the Bragg's order, and θ_i is the incident angle. The effective refractive index of n_{eff} was calculated by the sphere volume fraction of 0.74, the refractive index n_{SiO_2} of 1.447, and n_{air} of 1.0. For the q^{th} -order sub-peak positions (λ_q) resulting from the finite opal layers and Si-substrate with much higher refractive index [73]-[74], an interference phase condition was applied,

$$\lambda_q = \frac{2n_{eff}T}{m} = \frac{2n_{eff}N_{layer}d_{hkl}}{N_{layer} - q} \quad (3.5),$$

where T is the opal film thickness and q is the zero or positive integers. The theoretical positions (open symbols) indicate a good agreement with the measured ones.

Next, λ_0 has been measured at the various oblique incident angles ($\theta_i = 0 \sim 50^\circ$). A 12-layer opal specimen created by 718 nm diameter spheres was used. In Figure 3.13(b), the resulting values are presented together with a theoretical curve calculated by Equation (3.4). As declining the angle, the measured λ_0 values show a blue-shift, and also well match with the theoretical ones of Equation (3.4).

The verified results indicate that the self-assembled opal has highly-ordered crystalline structure of monodisperse silica spheres. It may also be utilized to extract the characteristics of PCs from the acquired peak information, such as the stopband position, opal thickness, sphere diameter, and the refractive index of silica sphere.

Chapter IV: Self-assembled Photonic Crystal Waveguides

4.1 Introduction

Photonic crystals (PCs) with photonic bandgap (PBG) [1]-[2] have been investigated widely, and may be incorporated into various integrated photonic devices including optical filters, sharp bending light guides, and very low threshold lasers [75]-[77]. Using nanofabrication processes, PCs of the two-dimensional (2-D) slab-type and three-dimensional (3-D) layer-by-layer structures can be built [4], [78]-[80]. Simpler and cheaper alternatives are the self-assembled PCs (inverse opals) with full 3-D PBG [8]-[9], [81]. Self-assembled opals with pseudo-PBG are used as the template, and are removed after infiltration of high refractive index materials. A defect in the PCs, which allows light localization, is required to realize integrated photonic functional devices [82]-[83].

In this chapter, first, a rib-type Si_3N_4 waveguide surrounded by the self-assembled silica opals is presented, which possesses a pseudo-PBG at the fiber communication wavelength. The conventional dielectric waveguide structure is designed and fabricated to be inserted into the opals without any critical disorder. The used fabrication processes and measurement results (e.g. propagation loss and transmission spectrum) are discussed. Next, the silicon infiltrated inverse opals with an omnidirectional full-PBG are utilized in the applications of planar- and line-defect waveguides. The fabricated defects are completely surrounded by the inverse opals. The microfabrication technology including microelectro-mechanical systems (MEMS) process technique and the self-assembly

technique of Chapter 2 are employed to build it.

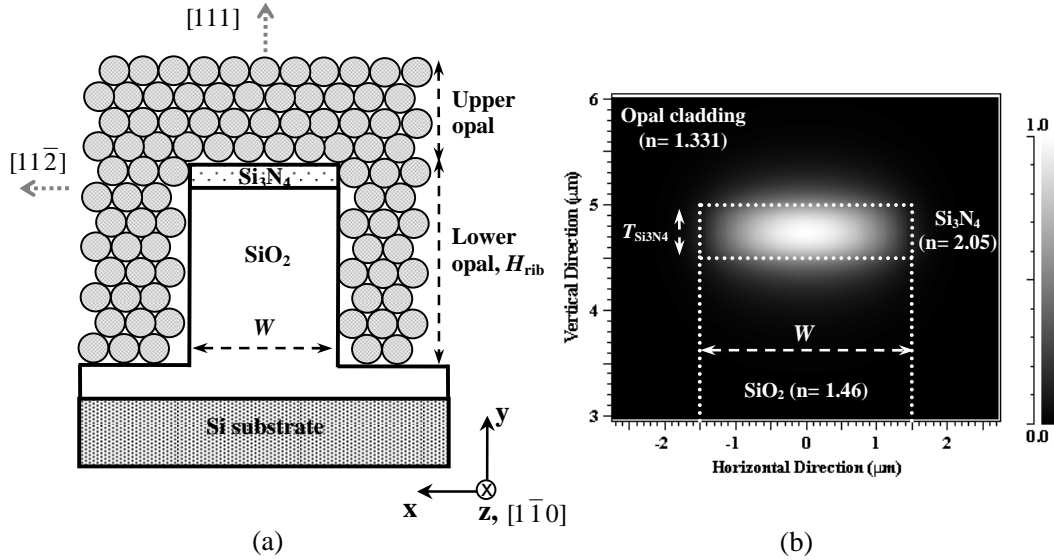


Figure 4.1 (a) Schematic of opal-clad Si_3N_4 waveguide; (b) mode profile (normalized electric field distribution at 1550 nm in wavelength) calculated by the imaginary distance beam propagation method: The dotted lines represent the Si_3N_4 waveguide structure ($3.0 \times 0.5 \mu\text{m}^2$). The effective refractive index of 1.331 was used for the cladding. Extended field near the top boundary of guide (i.e., [111] direction of opal) was also observed.

4.2 Opal-clad optical waveguide

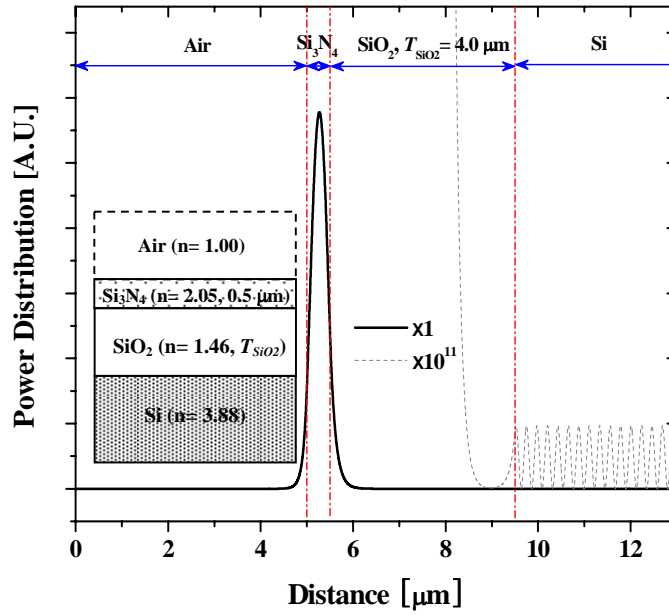
A rectangular channel Si_3N_4 waveguide supported by a SiO_2 rib has been utilized to build the opal-clad optical waveguide. As seen in Figure 4.1(a), the Si_3N_4 guide is isolated by the rib with an equal width (W) to the guide and an enough height (H_{rib}), in order to provide a required space to form an opal-clad and a minimized leakage to the Si-substrate induced by its higher refractive index. Its dimensions ($W \times H_{\text{rib}}$) become important factors for the complete opal-clad deposition without any mismatching

between the upper- and lower-opal layers. The crystalline directions of $[111]$ and $[11\bar{2}]$ are perpendicularly oriented to the top (y -direction) and side (x -direction) surface of guide, respectively, and the $[1\bar{1}0]$ points out the propagation direction of z [73].

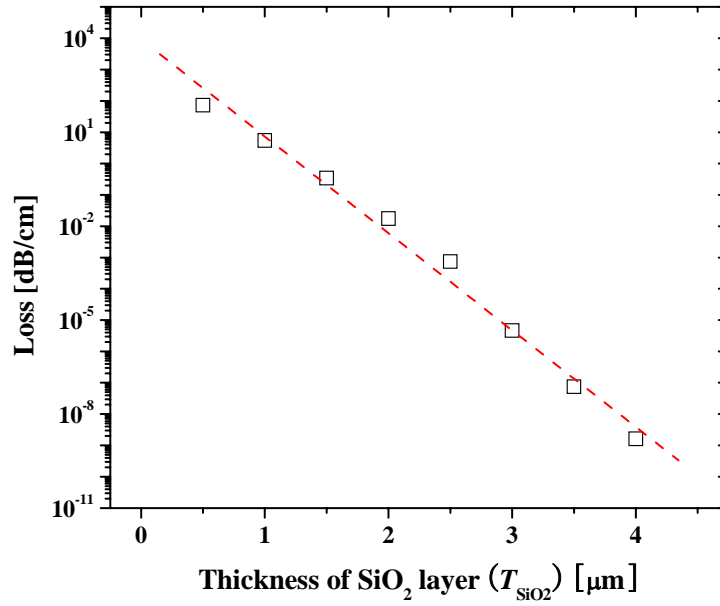
4.2.1 Rib-type waveguide structure

The modes of Si_3N_4 guide were first calculated at 1550 nm wavelength by the imaginary distance beam propagation method [84]. The n_{eff} of 1.331 for the opal-clad (as obtained in Section 3.4), $n_{\text{Si}_3\text{N}_4}$ of 2.05 for the guide, and n_{SiO_2} of 1.46 for the supporting rib were employed. Figure 4.1(b) depicts the fundamental mode profile (normalized electric field distribution) of Si_3N_4 guide with $W= 3.0 \mu\text{m}$ and a thickness ($T_{\text{Si}_3\text{N}_4}$) of $0.5 \mu\text{m}$, where single-mode propagation is observed. The mode shows an extended field distribution to the respective boundaries of guide. The PBG of opals is not omnidirectional and placed only in the Γ -L direction (i.e. only $[111]$ crystalline direction), as described in Section 2.2.2. Therefore, the top one may practically experience a unique PBG behavior as propagated through the guide, but the others not.

In optoelectronic devices based on a silicon technology, a thick SiO_2 buffer layer on top of the higher index Si-substrate is required to control the power leakage to the substrate as in [85]-[87], where 3~ 10 μm thick SiO_2 buffer layer has been employed. For the buffer layer design, the leakage loss to the Si-substrate was analytically calculated using a simple and efficient transfer matrix technique [88]-[89]. It may solve the Helmholtz equations to the planar multilayer structure (e.g. insert of Figure 4.2(a)) and



(a)



(b)

Figure 4.2 Leakage loss analysis of the planar multilayer structure (insert of (a)) using transfer matrix technique: (a) field distribution in case of $T_{SiO_2} = 4.0 \mu\text{m}$: The magnified oscillation field represents the leakage to the Si- substrate; (b) leakage losses as a function of the thickness of buffer layer (T_{SiO_2}).

obtain the field distribution and complex propagation constant (β), of which the imaginary part determines the magnitude of leakage ($\alpha_{WG} = 2\beta_{im}$) toward the substrate. Figure 4.2(a) shows the overall power distribution of the multilayer with $T_{Si_3N_4} = 4 \mu\text{m}$, and the oscillation (i.e. leakage loss) is observed. The α_{WG} as a function of T_{SiO_2} is depicted in Figure 4.2(b), which shows a monotonic decrease on a dB/cm scale. Eventually, a SiO_2 buffer layer of $6.0 \mu\text{m}$ was chosen for the rib-type waveguide to provide an enough space for the opal-clad and completely suppress the leakage loss.

The other critical dimensions (i.e. W and H_{rib}) may be determined by the size of silica spheres ($D = 713 \text{ nm}$ obtained in Section 2.2.2). The H_{rib} of $4.7 \mu\text{m}$ (i.e. substitution of 8-layer opals) and the W of $2.4 \mu\text{m}$ and $9.1 \mu\text{m}$ (i.e. substitution of 4- and 15-row opals) have initially been chosen.

4.2.2 Micro-fabrications & SEM characterizations

The designed rib-type waveguide has been built by the silicon based microfabrication technology, as shown in Figure 4.3. First, a $6.0 \mu\text{m}$ thick SiO_2 buffer layer was thermally grown on the Si-substrate at $1150 \text{ }^\circ\text{C}$, and a $0.45 \mu\text{m}$ thick Si_3N_4 layer was deposited by plasma enhanced chemical vapor deposition (PECVD) at $340 \text{ }^\circ\text{C}$. To build a pattern of $4.7 \mu\text{m}$ high rib (i.e. $0.45 \mu\text{m}$ of Si_3N_4 and $4.25 \mu\text{m}$ of SiO_2), the layers were anisotropically etched by reactive ion etching (RIE, CF_4 and CHF_3 gases used) after an optical lithography step. The process time of RIE was too long to use general polymeric etch-mask, which tends to be etched by the reactive gases. As an alternative, 1000 \AA thick aluminum hard mask was employed. The long process time

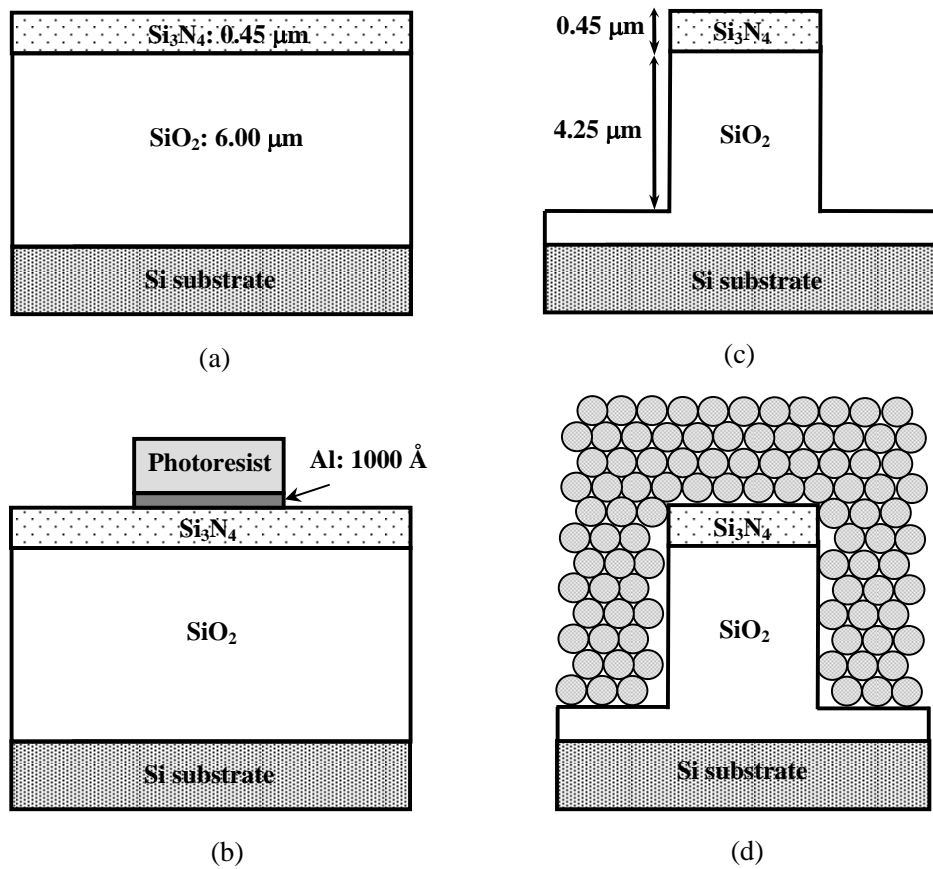


Figure 4.3 Opal-clad waveguide fabrication processes: (a) thermal oxidation for 6 μm thick SiO₂ layer and PECVD deposition for 0.45 μm thick Si₃N₄ layer; (b) e-beam evaporation for 1000 Å thick aluminum hard mask and photolithography; (c) RIE for rib patterning and chemical wet polishing; (d) self-assembly of silica spheres ($D= 703$ nm of Sec. 3.2.2).

also made the etched surface profile worse, which may induce scattering loss which degrades the performance of waveguides. The rough surface could fairly be improved by a chemical wet-polishing process (i.e. buffered hydrofluoric acid (HF) and phosphoric acid (H₃PO₄)). Subsequently, the prepared silica spheres ($D= 703$ nm ± 1.6 % of Section 3.2) are coated on the waveguide through the convective self-assembly method of Section

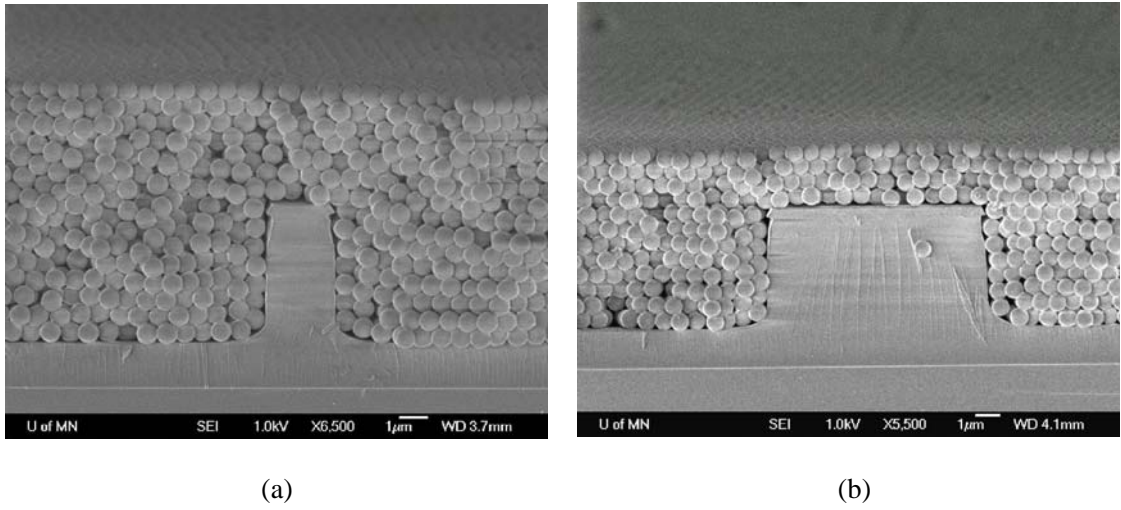


Figure 4.4 Cross sectional SEM images of the opal-clad waveguides: (a) $W= 2.3 \mu\text{m}$ (4-row substitution); (b) $W= 8.9 \mu\text{m}$ (15-row substitution): The practical H_{rib} is of $4.74 \mu\text{m}$ (substitution of 8-layer opals, $T_{SiO_2}= 4.3 \mu\text{m}$ and $T_{Si_3N_4}= 0.44 \mu\text{m}$). The measured dimensions show some slight deviation with the actual designed ones, and it may cause by the long RIE process time and the extra chemical wet-polishing. Uniform top surface and *fcc* closed packed arrangement are observed without any critical disorder near the guide.

3.3.1, and may eventually form the opal-cladding.

Figure 4.4 represents cross sectional SEM images of the fabricated opal-clad waveguides, where H_{rib} is of $4.74 \mu\text{m}$ ($T_{SiO_2}= 4.3 \mu\text{m}$, $T_{Si_3N_4}= 0.44 \mu\text{m}$), and W s are of $2.3 \mu\text{m}$ and $8.9 \mu\text{m}$, respectively. The measured dimensions show some slight deviation with the actual designed ones, and it may cause by the long RIE process time and the extra chemical wet-polishing. The self-assembled opal-cladding possesses a uniform top surface of *fcc* closed-packed arrangement without any critical crack or disorder near the guide. It indicates that the self-assembly technique may be suitable for non-planar structure coatings as well [73].

4.2.3 Optical characterizations

4.2.3.1 Propagation loss measurements

Propagation losses of optical waveguide may be classified as absorption, radiation and scattering losses, and in case of the dielectric waveguides, the scattering loss (especially induced at the surface of guide) is fairly dominant [90]. To quantitatively describe the loss, the associated attenuation coefficient (α) is generally used as follows:

$$P(z = L) = P(z = 0) \cdot e^{-\alpha \cdot z} \quad (4.1),$$

$$4.343 \times \alpha = \frac{10 \log_{10}(P(L)/P(0))}{L} \text{ [dB/cm]} \quad (4.2),$$

where P is the optical power at a certain position (z) along the waveguide, and L is the length of waveguide. Based on Equation (4.2), the practical propagation loss may be characterized through measuring the transmitted powers as a function of L , of which the slope and the y -intercept represent its propagation and coupling (insertion) losses, respectively. To vary the L , the waveguide can be repetitively shortened by cleaving and polishing, referred to as cutback method.

For the loss measurement, a simple direct-coupling (called end-fire coupling) technique was employed, which is to launch a focused light signal onto the polished facet of guide and detect the output power transmitted through the waveguide. The measurement setup consists of laser sources of $\lambda = 1465$ nm and 1532 nm, optical detector, power meter, IR CCD camera, multi-axis linear stage controlled by motorized actuators, and other trivial optical components.

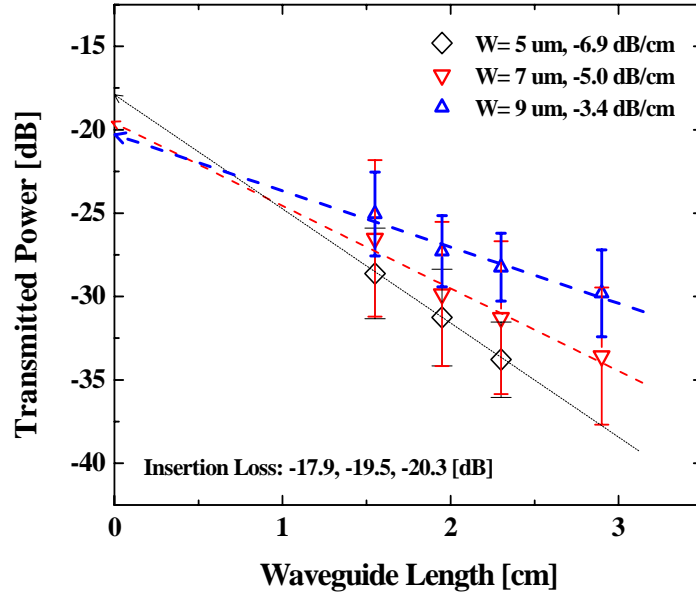
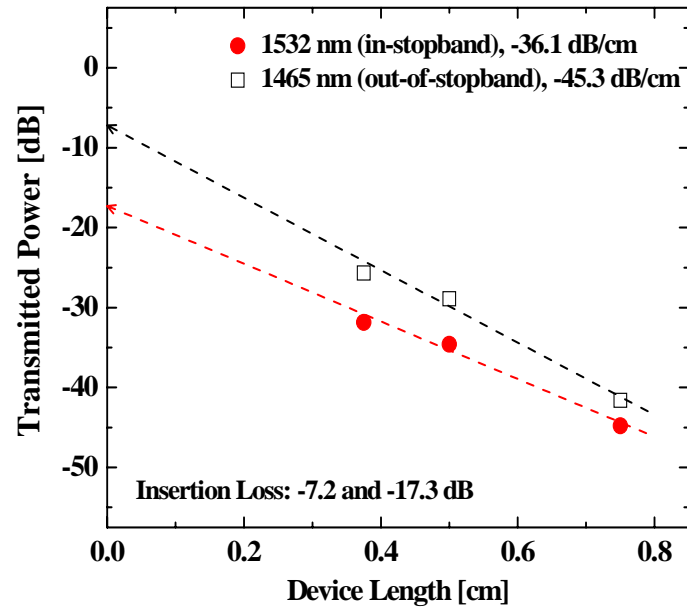


Figure 4.5 Propagation loss measurement results depending on the width ($W= 5, 7,$ and $9 \mu\text{m}$) and length ($L= 1.5\sim 3.0 \text{ cm}$) of rib waveguide. The slop and y-intercept represent its propagation and coupling (insertion) losses, respectively.

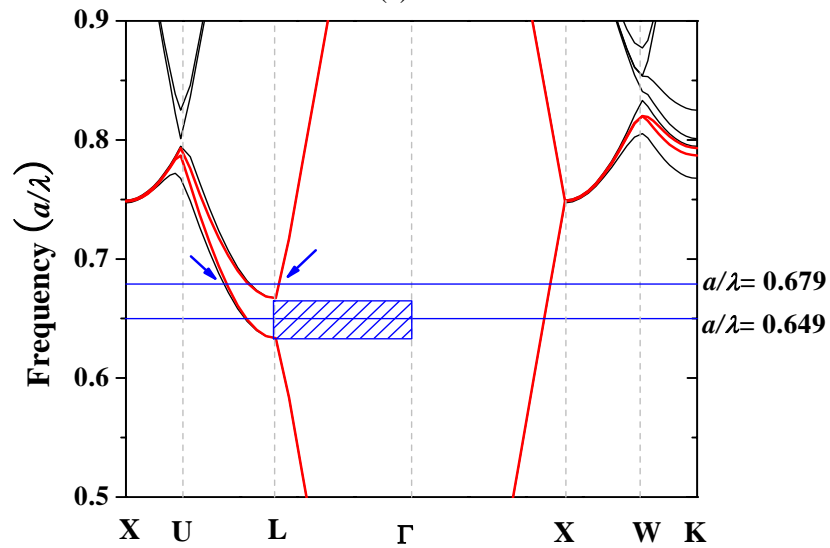
Initially, the losses of rib waveguides were measured, of which W (approximate $5, 7,$ and $9\text{-}\mu\text{m}$) and L ($1.5\sim 3.0 \text{ cm}$) were varied. The measurements were repeated for $5\sim 10$ samples by the identical setup and method, and the average transmitted powers are shown in Figure 4.5. The propagation losses of $3.4\sim 6.9 \text{ dB/cm}$ and insertion loss of about 19 dB were extracted. The measurement result also follows the theoretical scattering loss model of [91]:

$$\alpha = 4(k\sigma)^2 \left(\frac{\cos^3 \theta}{\sin \theta} \right) \frac{1}{W + 2/p} \quad (4.3),$$

where k is the propagation constant, σ is the surface roughness, θ is the propagation angle of light, and p is decay constant in the cladding.



(a)



(b)

Figure 4.6 (a) Measured propagation losses of the opal-clad waveguide ($W= 8.9 \mu\text{m}$) at $\lambda= 1532 \text{ nm}$ (36.1 dB/cm, in-stopband, $a/\lambda= 0.649$) and 1465 nm (45.3 dB/cm, out-of-stopband, $a/\lambda= 0.679$): The insertion loss at 1532 nm is much higher than at 1465 nm ; (b) photonic bandstructure of opals near the PBG (hatched area): It shows that two more opal modes (indicated by arrows) exist at $a/\lambda= 0.679$ and in the respective Γ -L and L-U directions (i.e. oriented to the top and side surface of guide). The differences in the losses may be induced by the opal PBG and bulk modes.

Next, the opal-clad waveguide ($W= 8.9 \mu\text{m}$) was characterized by the same method as well, as shown in Figure 4.6(a). At the respective $\lambda= 1532 \text{ nm}$ (in-stopband, $a/\lambda= 0.649$) and 1465 nm (out-of-stopband, $a/\lambda= 0.679$), the propagation losses of 36.1 dB/cm and 45.3 dB/cm were extracted, and at $\lambda= 1532 \text{ nm}$ the much enhanced loss by 9.2 dB/cm is obtained. On the other hand, the insertion loss at $\lambda= 1532 \text{ nm}$ (17.3 dB) is much higher than at $\lambda= 1465 \text{ nm}$ (7.2 dB). The opal-clad waveguide shows much higher loss than the intrinsic one of rib waveguide, and it may result from the silica spheres adjacent to the guide, which originally act as scattering centers. The opal cladding may control only the $[111]$ directional light, but otherwise scatter and escape from the guide.

Figure 4.6(b) depicts the band structure of opals near the PBG, and two extra opal bulk modes (i.e. leaky modes) are observed at $a/\lambda= 0.679$ (out-of-PBG) in the respective Γ - L and L - U directions corresponding to $[111]$ and $[11\bar{2}]$ as shown in Figure 4.1(a). The deviations of in- and out-of-stopband losses may be mainly induced by the PBG behavior and the extra leaky modes of opals.

4.2.3.2 Transmission spectrum measurement

To explore the PBG behavior of the opal cladding at the waveguide in detail, a transmission spectrum was measured using a tunable laser source and the identical measurement setup. The opal-clad waveguide is of $W= 8.9\text{-}\mu\text{m}$ and $L= 0.7\text{-cm}$. In Figure 4.7(a), a maximum peak (λ_o^T) of 1532 nm within the opal stopband (hatched area, $\lambda= 1491\sim 1568 \text{ nm}$) and other sub-peaks (out-of-stopband) are observed, which may be

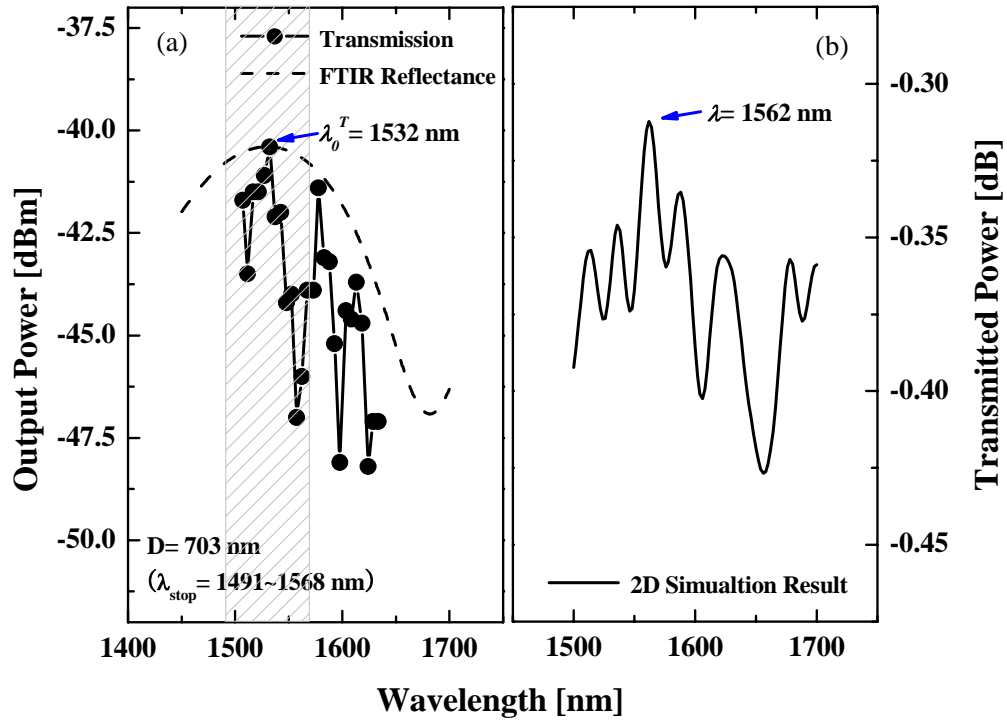


Figure 4.7 (a) Measured transmission spectrum of 8.9 μm wide and 0.7 cm long opal-clad waveguide. It shows maximum transmission peak wavelength (λ_0^T) of 1532 nm and other sub-peaks. A dashed line represents the FTIR opal spectrum of Sec. 3.4, which is scaled by decibel to compare with the waveguide result. The opals with $D=703$ nm possess a stopband (hatched area) of 1491~1568 nm; (b) calculated spectrum by 2-D (yz plane) as shown in Figure 4.1(a) simulation using imaginary distance beam propagation technique.

attributed to the defect guided mode of in-PBG and index guided mode of out-of-PBG, respectively, as described in Chapter 2. The λ_0^T fairly agrees with the previously calculated and measured λ_0 of opals as well. A dashed line of Figure 4.7(a) represents the FTIR opal spectrum of Section 3.4, which is scaled by decibel to compare with the waveguide result. The FTIR result of 4-layer opals forms an envelope of the transmission spectrum. Figure 4.7(b) shows a simulation result calculated by imaginary

distance beam propagation technique. The calculated spectrum shows a similar profile to the measured except for a slight shift in wavelength. It may be due to using a 2- D hexagonal closed packed structure instead of the actual 3- D fcc closed packed structure in the simulation.

4.3 Embedded defect structures in α -Si inverse opals

In this section, two types of embedded defect structures in the self-assembled PCs with a complete PBG near $\lambda = 1550$ nm are discussed. A planar defect of a Si_3N_4 layer and a line defect of a rectangular channel-type Si-waveguide are placed into the inverse opals comprising of air spheres and interstitial α -Si, as shown in Figure 4.8. The defects are initially fabricated, and then the α -Si inverse opals are formed around the defect.

The dimension ($W \times H$) of the channel waveguide is totally dependent on the size of sphere, and for example, in case of the silica spheres of $D = 870$ nm and 1-row and 1-layer substitution, W of 0.64- μm and H of 0.55- μm are required to be naturally inserted into the inverse opals, as specified in Section 2.2.2.

Microfabrication technology including the MEMS process technique has been employed [92]. The low- σ Si_3N_4 layers depicted in the Figure 4.8(a) and (c) are utilized not only as a planar defect but also a etch stop layer to build the free-standing inverse opal membrane. It can be released from the Si-substrate through a potassium hydroxide (KOH) etch process, where the etch rate of the silicon $\langle 111 \rangle$ plane is much slower than other plane and sidewalls of 54.7° are formed.

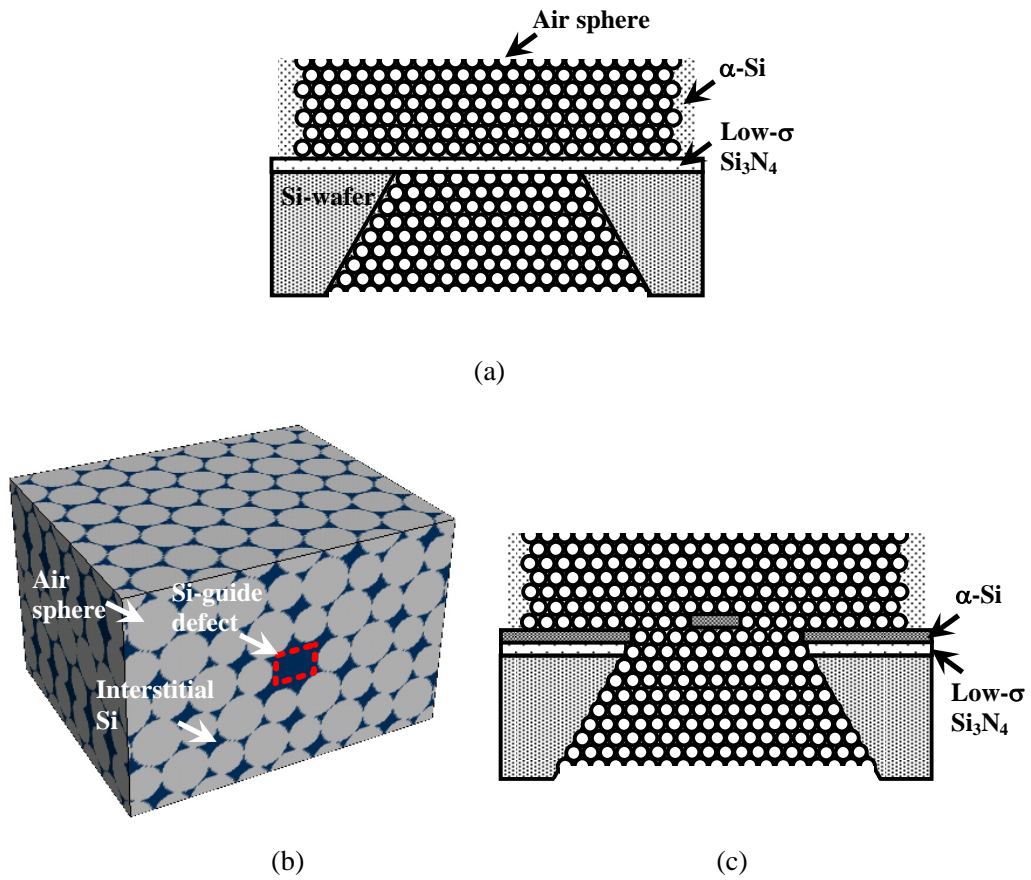


Figure 4.8 Schematics of embedded defect structures in α -Si inverse opals: (a) planar defect structure; (b) line defect of rectangular channel Si-waveguide ($W= 0.64\text{-}\mu\text{m}$, $H= 0.55\text{-}\mu\text{m}$, 1-row and 1-layer substitution); (c) cross sectional view of line-defect (3-row and 1-layer substitution): The air spheres are of $D= 870\text{ nm}$ and the self-assembled inverse opals have a complete PBG near 1550 nm , as specified in Sec. 2.2.2.

4.3.1 Planar-defect Si_3N_4 layer

The fabrication of embedded Si_3N_4 planar defect begins with a low-pressure chemical vapor deposition (LPCVD) of $1\text{ }\mu\text{m}$ thick low- σ Si_3N_4 on the double side polished (100)-Si wafer. After backside photolithography and RIE of the Si_3N_4 layer

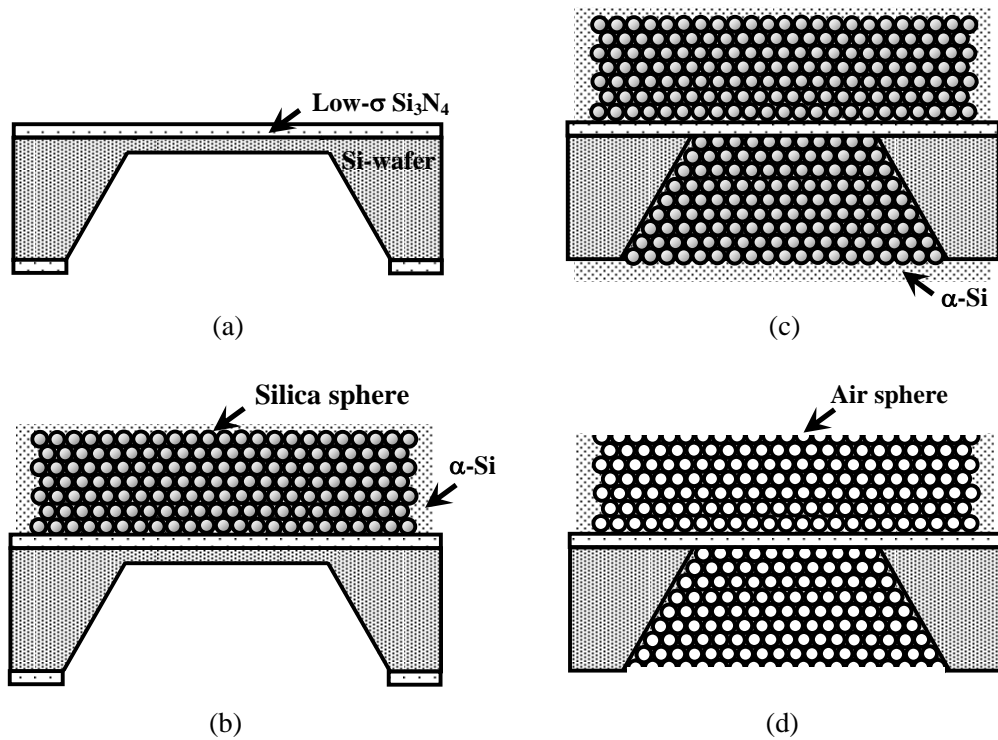


Figure 4.9 Fabrication process flow of planar defect: (a) LPCVD of 1- μm thick low- σ Si_3N_4 and first KOH etching of Si-substrate backside; (b) first self-assembly of silica spheres and first LPCVD for α -Si infiltration; (c) second KOH etching of the remained Si-substrate (10~ 20 μm thickness), second self-assembling, and second α -Si LPCVD; (d) RIE and HF wet-etching for removing silica spheres.

which also acts as a KOH-blocking mask, a KOH Si-etching process is performed, and a deep trench and 10~ 20 μm thick supporting layer are left, as shown in Figure 4.9(a). At this process step, a dilute KOH (30~ 45 wt%, 80 °C) is utilized for the anisotropic etch process. Subsequently, silica spheres of $D= 853$ nm and α -Si are self-assembled and infiltrated (Figure 4.9 (b)) by the techniques described in Section 3.3. Figure 4.9(c) and (d) shows the rest of processes in detail (i.e. the second KOH etching of the remained Si-substrate, self-assembling, LPCVD of α -Si infiltration, and final RIE and HF wet etching

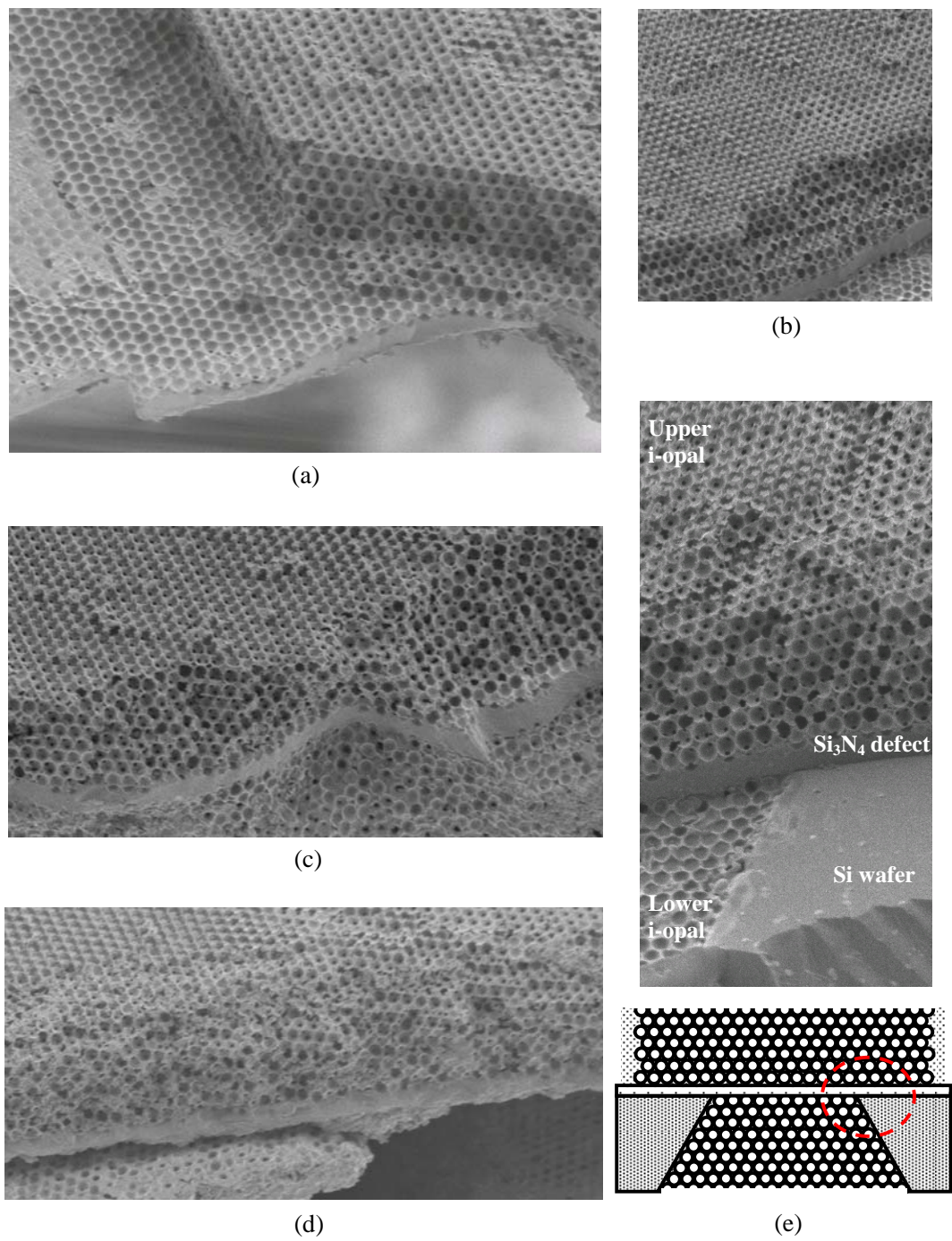


Figure 4.10 SEM images of a planar defect (1 μm thick low- σ Si_3N_4 layer) embedded in the inverse opals: (a) and (b) top-views of upper inverse opal; (c), (d), and (e) cross sectional views and a schematic.

to form air spheres). At the second KOH etching step, the bunch of KOH droplets are filled into the trench and then heated to completely remove the remained Si-substrate.

Figure 4.10 depicts some SEM images of the embedded planar defect. The observed inverse opals exhibits an *fcc* close packed arrangement without any critical crack or disorder, and the Si_3N_4 planar defect is inserted between the upper- and lower-inverse opals. Eventually, the bottom-released α -Si infiltrated opal membrane makes it feasible to complete the embedded defect structure, and this technique may be employed in the other self-assembled PC applications.

4.3.2 Line-defect α -Si waveguide

The embedded line-defect α -Si waveguide has been fabricated utilizing the membrane technique as well. Figure 4.11 presents its overall fabrication process flow, and the main processes, for the most parts, are identical with ones utilized in Section 4.3.1. Some additional process steps are performed to pattern a line defect and completely release the infiltrated opals and line defect, as shown Figure 4.11(b) and (d).

The fabrication of the line defect waveguide starts with LPCVD of α -Si (7000 Å) on the low- σ Si_3N_4 layer, and conventional photolithography and RIE steps are followed. The defect dimensions of $H=0.55\ \mu\text{m}$ (1-layer substitution) and several appropriate W (n -row substitution) are chosen to substitute the removed inverse opals. Figure 4.12(a) present the SEM image of self-assembled silica spheres on the line defect ($W=9.0\ \mu\text{m}$, $H=0.55\ \mu\text{m}$, 12-row and 1-layer substitution). The self-assembled opals also possess a good *fcc* close packed arrangement, and it shows that the defect is successfully inserted

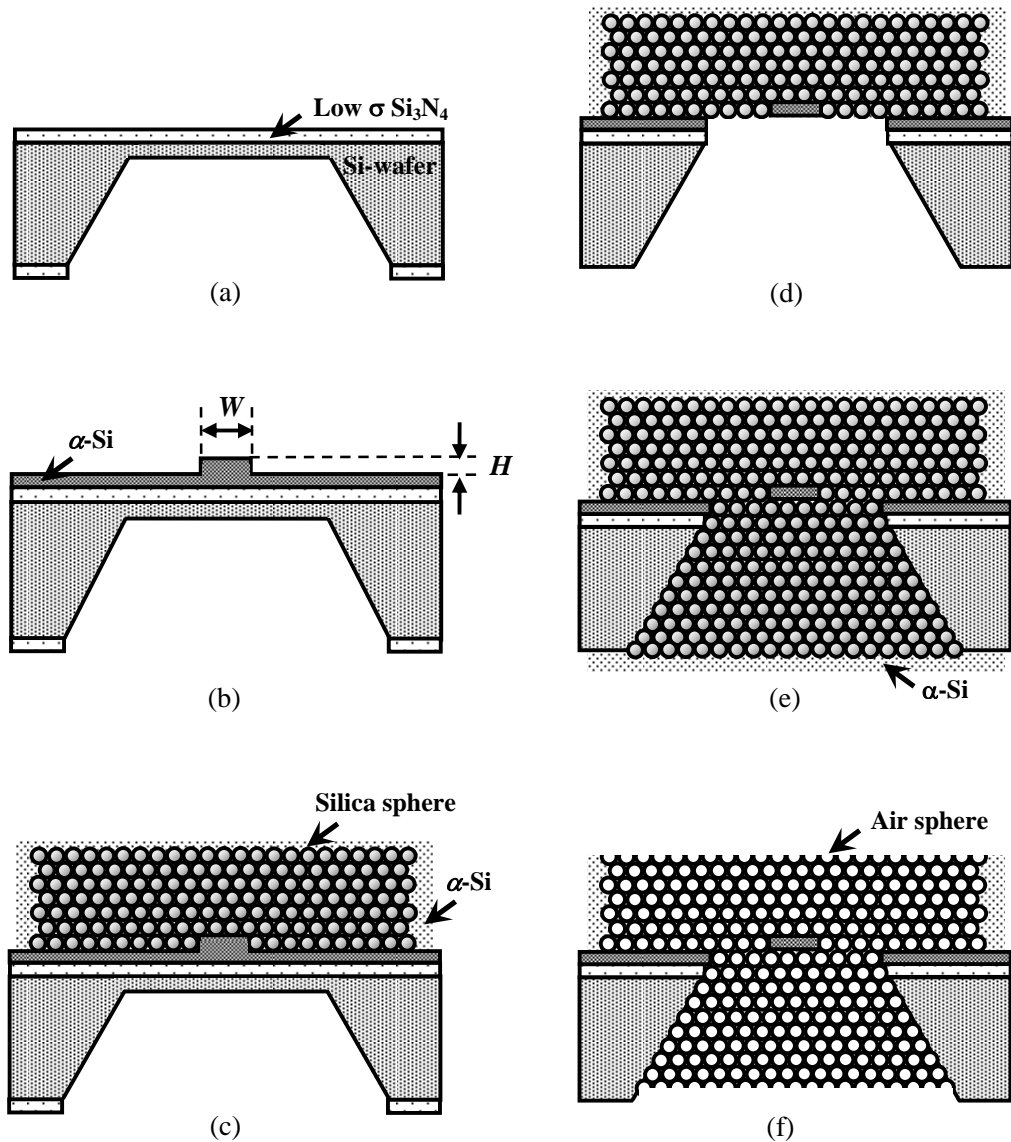
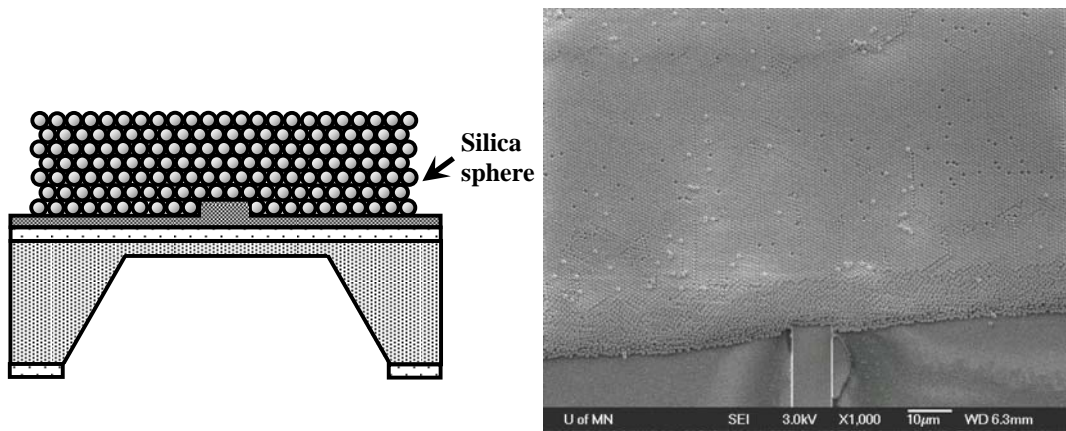
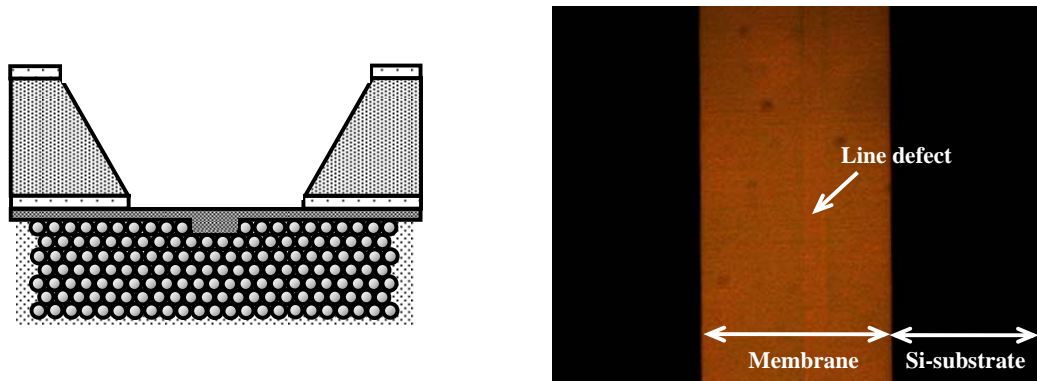


Figure 4.11 Schematics of the fabrication process flow: (a) LPCVD of 1 μm thick low- σ Si_3N_4 and 1st KOH etching of Si-substrate; (b) LPCVD of 7000 \AA thick α -Si and RIE for defect patterning; (c) first self-assembly of silica spheres, and first LPCVD for α -Si infiltration; (d) second KOH etching of the remained Si-substrate (10~ 20 μm) and subsequent RIE of low- σ Si_3N_4 and α -Si; (e) second self-assembly of silica spheres, and second LPCVD for α -Si infiltration; (f) RIE and HF wet etching for removing silica



(a)



(b)

Figure 4.12 (a) Schematic and SEM image of self-assembled silica spheres on a line-defect ($W= 9.0 \mu\text{m}$, $H= 0.55 \mu\text{m}$, 12-row and 1-layer substitution); (b) schematic and microscopic image of Figure 11(d): It shows a free-standing membrane structure which is bottom-released from Si-substrate.

into the PC. For the lower inverse opals, the supporting layers (i.e. remained Si-substrate, a Si_3N_4 layer, and a $\alpha\text{-Si}$ layer underneath the line defect) are successively etched, and therefore the $\alpha\text{-Si}$ infiltrated opals and line defect can be bottom-released, as shown in Figure 4.12(b).

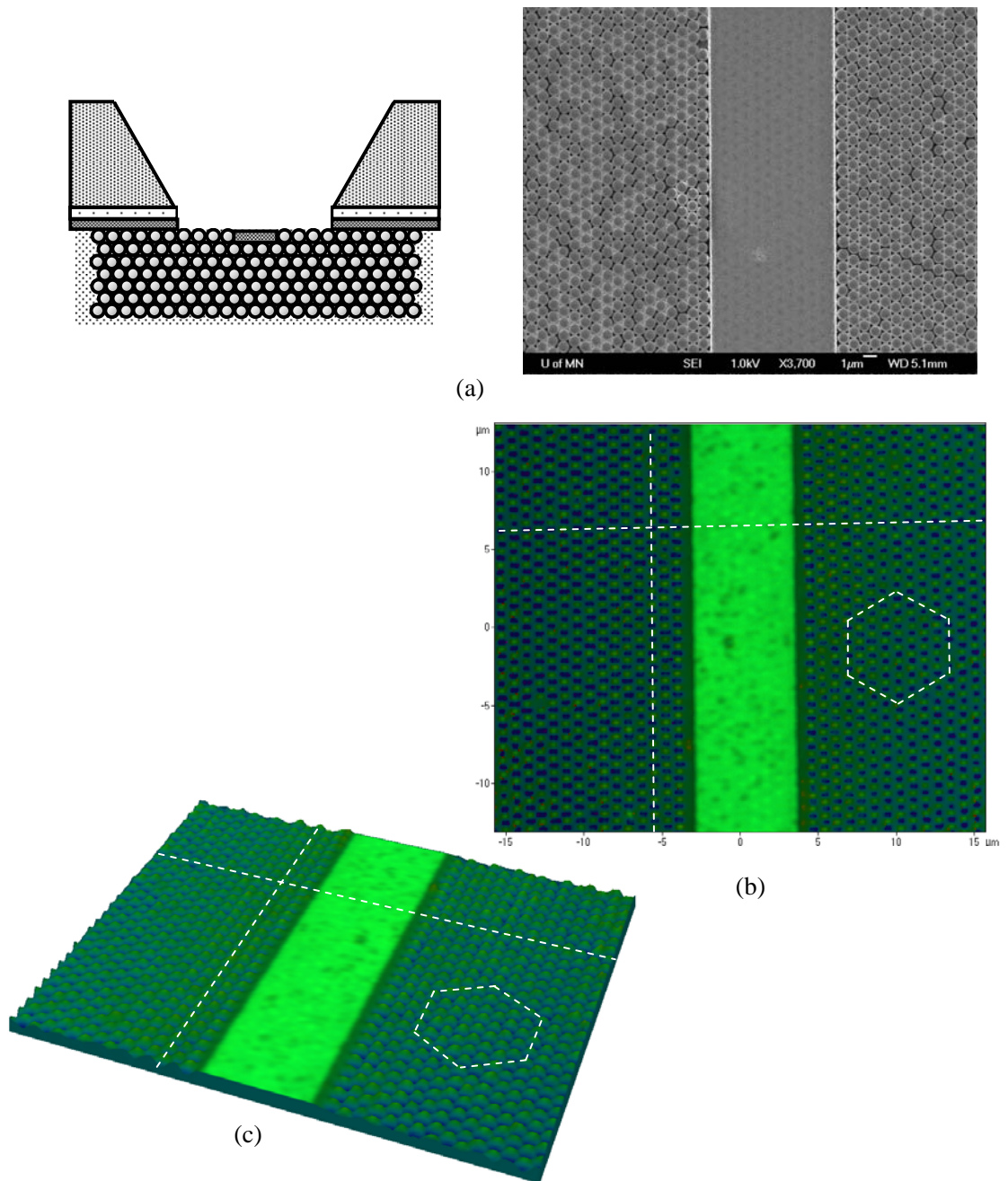
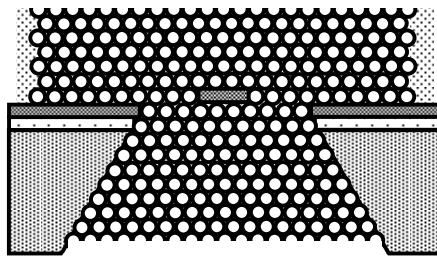


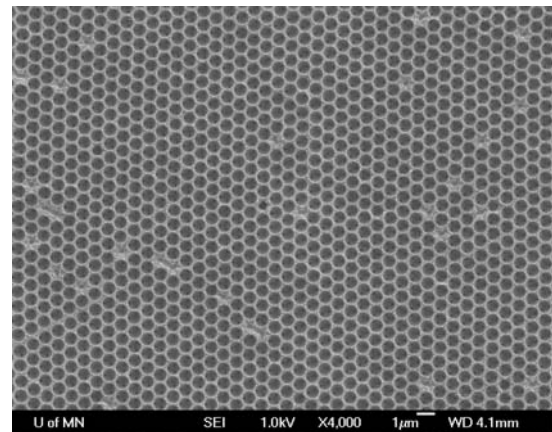
Figure 4.13 (a) Schematic and SEM image of the completely released opal membrane and an inserted line defect ($W= 9.0 \mu\text{m}$, 12-row substitution); (b) & (c) confocal microscopic images ($30 \mu\text{m} \times 30 \mu\text{m}$) of 2-D top-view and 3-D geometry: Si-waveguide ($W= 7.5 \mu\text{m}$, 10-row substitution) is inserted in Si-infiltrated opals and embossed-patterns (hexagonal-close-packed) of exposed silica spheres are clearly observed.

Figure 4.13 presents a SEM image and confocal microscopic images of the opal membrane and inserted line defect. In Figure 4.13(b) and (c), a Si-waveguide ($W=7.5\ \mu\text{m}$, 10-row substitution) inserted in the infiltrated opals is shown, and periodically arranged hexagonal-close-packed pattern of the exposed silica spheres are clearly observed.

After the backside processes, the embedded line-defect within the inverse opal can be produced, as depicted in Figure 4.14. The cross sectional view of the final line-defect waveguide structure is not available in this dissertation. The prepared specimens were confronted with a cleaving trouble (i.e. breaks induced by the coarse specimen fixture), which has not occurred in the case of the planar-defect. Its failure analysis or a reliable alternative for the cleaving is required to enable its optical characterizations.



(a)



(b)

Figure 4.14: Schematic (a) and SEM top-view image (b) of the fabricated α -Si waveguide embedded within the inverse opals.

Chapter 5: Conclusions and Future Work

In this dissertation, the optical waveguide applications utilizing the 3-D self-assembled PCs have been discussed. The various theoretical and experimental results have been provided and correlated. The results show that the self-assembled opal and inverse opal are feasible to be applied in the integrated optics and photonics.

The photonic bandstructures of the self-assembled PCs were calculated through the PWE method, and their pseudo- and omnidirectional full-PBG were obtained. For the PC applications near 1550 nm, the respective sizes of silica and air spheres were chosen. For the band calculation of the embedded α -Si waveguide in the inverse opals, the supercell method was used, and its guided defect modes within the PBG as well as the bandstructure were successfully obtained. The 3-D FDTD simulations were performed to characterize and evaluate the unique properties and performance of the PC waveguide. Under the optimized computational conditions, the transmitted power and propagation loss spectra were calculated. The stopband signals showed the low-loss propagation through the defective Si-waveguide due to the PBG effect. The transmitted power spectrum from the FDTD calculation was compared with the corresponding band structure, and the results were correlatable.

To build the PCs with a highly-ordered *fcc* closed-packed arrangement and a stopband near 1550 nm wavelength, the large monosized silica spheres were initially prepared through the developed efficient fast-growth method. The subsequent preannealing and centrifuge collection process provided the shrink-proof and high-purity

colloidal spheres after removing the aggregates. The large-sized colloidal spheres in the pure ethanol or aqueous 1-propanol mixture were successfully self-assembled by the convective method or convective method assisted by the Marangoni effect. For the inverse opal with the complete PBG, the α -Si LPCVD infiltration and selective etchings were additionally performed. The produced self-assembled PCs were optically characterized by SEM inspection and FTIR spectroscopy, and had the highly-ordered crystalline structure and the stopband near 1550 nm wavelength.

The self-assembled PCs were incorporated with three types of defect structures. The opal-clad waveguide was fabricated and characterized. The opal cladding surrounding Si₃N₄ guide was built by the self-assembly of colloidal silica spheres. The correlated theoretical and experimental results verify that the pseudo-PBG of opals exists near $\lambda = 1532$ nm, and the propagation loss of 36.1 dB/cm was measured. The embedded planar- and line-defect in the inverse opals with an omnidirectional and complete PBG were fabricated by utilizing the MEMS process technology as well. The suggested membrane technique may be employed in the various applications of the self-assembled PCs.

As further studies on the embedded line-defect waveguide in the inverse opals, a reliable specimen cleaving technique and its optical characterizations are required. Replacing the Si-waveguide with a laser waveguide structure in AlGaAs/GaAs or InGaAs/InP would enable investigations of the PBG cladding effect for the laser application.

Bibliography

- [1] E. Yablonovitch, "Inhibited spontaneous emission in solid-state physics and electronics," *Phys. Rev. Lett.*, vol. 58, pp. 2059-2062, May 1987.
- [2] S. John, "Strong localization of photons in certain disordered dielectric sperlattices," *Phys. Rev. Lett.*, vol. 58, pp. 2486-2489, Jun. 1987.
- [3] J. D. Joannopoulos, *Photonic crystals: Molding the flow of light*. Princeton, NJ: Princeton Univ. Press, 1995.
- [4] S.J. McNab, N. Moll, Y.A. Vlasov, "Ultra-low loss photonic integrated circuit with membrane-type photonic crystal waveguides," *Opt. Express*, vol. 22, pp. 2927-2939, Nov. 2003.
- [5] H.-G. Park, S.-H. Kim, S.-H. Kwon, Y.-G. Ju, J.-K. Yang, J.-H. Baek, S.-B. Kim, Y.-H. Lee, "Electrically driven single-cell photonic crystal laser," *Science*, vol. 305, pp. 1444-1447, Sep 2004.
- [6] M. Makarova, V. Sih, J. Warga, R. Li, L. dal Negro, J. Vuckovic, "Enhanced light emission in photonic crystal nanocavities with Erbium doped silicon nanocrystals," *Applied Physics Letters*, vol. 92, pp. 161107-1-161107-3, 2008.
- [7] K. Busch, and S. John, "Photonic band gap formation in certain self-organizing systems," *Phys. Rev. E*, vol. 58, n. 3, pp. 3896-3908, 1998.
- [8] A. Blanco, E. Chomski, S. Grabtchak, M. Ibisate, S. John, S.W. Leonard, C. Lopez, F. Meseguer, H. Miguez, J.P. Mondia, G.A. Ozin, O. Toader, H.M. van Driel, "Large-scale synthesis of a silicon photonic crystal with a complete three-dimensional bandgap near 1.5 micrometers," *Nature*, vol. 405, pp. 437-440, May 2000.
- [9] Y.A. Vlasov, X.-Z. Bo, J.C. Sturm, D.J. Norris, "On-chip natural assembly of silicon photonic bandgap crystals," *Nature*, vol. 414, pp. 289-293, Nov. 2001.
- [10] E. Vekris, V. Kitaev, G. Freymann, D. D. Perovic, J. S. Aitchison and G. A. Ozin, "Buried linear extrinsic defects in colloidal photonic crystals," *Adv. Mater.*, vol. 17, pp. 1269-1272, 2005.
- [11] Y. Jun, C.A. Leatherdale, D.J. Norris, "Tailoring air defects in self-assembled photonic bandgap crystals," *Adv. Mater.*, vol. 17, pp. 1908-1911, 2005.

- [12] S.A. Rinne, F. Garcia-Santanaria, P.V. Braun, "Embedded cavities and waveguides in three-dimensional silicon photonic crystals," *Nature Photonics*, vol. 2, pp. 52-56, Jan. 2008.
- [13] K. M. Ho, C. T. Chan, C. M. Soukoulis, "Existence of a photonic gap in periodic dielectric structures," *Phys. Rev. Lett.*, vol. 65, no. 25, pp. 3152-3155, 1990.
- [14] M. Plihal, A. A. Maradudin, "Photonic band structure of two-dimensional systems: The triangular lattice," *Phys. Rev. B*, vol. 44, no. 16, pp. 8565-8571, 1991.
- [15] P. R. Villeneuve, M. Piché, "Photonic band gaps in two-dimensional square and hexagonal lattices," *Phys. Rev. B*, vol. 46, no. 8, pp. 4969-4972, 1992.
- [16] R. D. Meade, K. D. Brommer, A. M. Rappe, J. D. Joannopoulos, "Existence of a photonic band gap in two dimensions," *Appl. Phys. Lett.*, vol. 61, no. 4, pp. 495-497, 1992.
- [17] A. Mekis, S. Fan, and J.D. Joannopoulos, "Bound states in photonic crystal waveguides and waveguide bends," *Phys. Rev. B*, vol. 58, n. 8, pp. 4809-4817, 1998.
- [18] W. C. Sailor, F. M. Mueller, and P. R. Villeneuve, "Augmented-plane-wave method for photonic band-gap materials," *Phys. Rev. B*, vol. 57, pp. 8819-8822, 1998.
- [19] S. Johnson and J. Joannopoulos, "Block-iterative frequency-domain methods for Maxwell's equations in a planewave basis," *Opt. Express*, vol. 8, no. 173, 2001.
- [20] J. B. Pendry and A. MacKinnon, "Calculation of photon dispersion relations," *Phys. Rev. Lett.*, vol. 69, pp. 2772-2775, 1992.
- [21] J. M. Elson and P. Tran, "Coupled-mode calculation with the R-matrix propagator for the dispersion of surface waves on truncated photonic crystal," *Phys. Rev. B*, vol. 54, pp. 1711-1715, 1996.
- [22] J. Chongjun, Q. Bai, Y. Miao, and Q. Ruhu, "Two-dimensional photonic band structure in the chiral medium transfer matrix method," *Opt. Commun.*, vol. 142, pp. 179-183, 1997.
- [23] S. Fan, "Sharp asymmetric line shapes in side-coupled waveguide-cavity systems," *Appl. Phys. Lett.*, vol. 80, pp. 908-910, 2002.
- [24] S. Fan, P. R. Villeneuve, and J. D. Joannopoulos, "Large omnidirectional band gaps in metallodielectric photonic crystals," *Phys. Rev. B*, vol. 54, pp. 11245-11251, 1996.

- [25] A. Tavlove, *Computational Electrodynamics: The Finite-Difference Time-Domain Method*. Norwood, MA: Artech House, 2000.
- [26] A. Chutinan and S. Noda, "Waveguide and waveguide bends in two-dimensional photonic crystal slabs," *Phys. Rev. B*, vol. 62, pp. 4488-4492, 2000.
- [27] T. Ochiai and K. Sakoda, "Dispersion relation and optical transmittance of a hexagonal photonic crystal slab," *Phys. Rev. B*, vol. 63, pp. 125107-125113, 2001.
- [28] M. Agio and C. M. Soukoulis, "Ministop bands in single-defect photonic crystal waveguides," *Phys. Rev. E*, vol. 64, pp 055603-1-055603-4, 2001.
- [29] Rsoft Design Group Inc., *BandSOLVE 2.0 user manual*. Ossining, NY, 2005.
- [30] Rsoft Design Group Inc., *FullWAVE 4.0 user guide*. Ossining, NY, 2005.
- [31] S.G. Johnson and J.D. Joannopoulos, *The MIT Photonic-Bands Package Homepage*, <http://ab-initio.mit.edu/mpb/>.
- [32] K. Sakoda and H. Shiroma, "Numerical method for localized defect modes in photonic lattices," *Phys. Rev. B*, vol. 56, pp. 4830-4835, 1997.
- [33] T. Sondergaard, "Spontaneous emission in two-dimensional photonic crystal microcavities," *IEEE J. of Quantum Elect.*, vol. 36, no. 4, pp. 450-547, 2000.
- [34] S.G. Johnson, J.D. Joannopoulos, *Photonic Crystals: The Road from Theory to Practice*. Boston, MA: Kluwer Academic Publishers, 2002.
- [35] V. Lousse, S. Fan, "Waveguides in inverted opal photonic crystals," *Optics Express*, vol. 14, no. 2, pp. 866-878, 2006.
- [36] M.D. Pagnoux, M.P. Fornel, *Photonic Crystals Towards Nanoscale Photonic Devices*. 2nd ed., Berlin: Springer, 2008.
- [37] K. Yee, "Numerical solution of initial boundary value problems involving Maxwell's equation sin isotropic media," *IEEE Transaction on Antennas and Propagation*, vol. 14, no. 3, pp. 302-307, 1966.
- [38] C. Lopez, "Material Aspects of Photonic Crystals," *Adv. Mater.*, vol. 15, no. 20, pp. 1679-1704, 2003.
- [39] H.S. Sozuer and J.W. Haus, "Photonic bands: Convergence problems with the plane-wave method" *Phys. Rev. B*, vol. 45, no. 24, pp. 13962-13972, 1992.

- [40] A. Lavrinenko, P. I. Borel, L. H. Frandsen, M. Thorhauge, A. Harpoth, M. Kristensen, T. Niemi, "Comprehensive FDTD modeling of photonic crystal waveguide components," *Optics Express*, vol. 12, no. 2, pp. 234-248, 2004.
- [41] R. S. Jacobsen, A. V. Lavrinenko, L. H. Frandsen, C. Peucheret, B. Zsigri, G. Moulin, J. Fage-pedersen, P. I. Borel, "Direct experimental and numerical determination of extremely high group indices in photonic crystal waveguides," *Optics Express*, vol. 13, no. 20, pp. 7861-7871, 2005.
- [42] G. Kolbe, "Das komplexchemische verhalten der kieselsaure: The complex chemical behavior of silica," *Ph.D. Dissertation*, Friedrich-Schiller-Universität Jena, Germany, 1956.
- [43] W. Stöber, A. Fink, E. Bohn, "Controlled growth of monodisperse silica spheres in the micron size range," *J. Colloid. Interf. Sci.*, vol. 26, pp. 62-69, 1968.
- [44] A. Van Blaaderen, J. Van Geest, A. Vrij, "Monodisperse colloidal silica spheres from tetraalkoxysilanes: Particle formation and growth mechanism," *J. Colloid. Interf. Sci.*, vol. 154, pp.481-501, 1992.
- [45] D.W. McComb, B.M. Treble, C.J. Smith, R.M. De La Rue and N. P. Johnson, "Synthesis and characterisation of photonic crystals," *J. Mater. Chem.*, vol. 11, pp.142-148, 2001.
- [46] C.G. Tan, B.D. Bowen, N. Epstein, "Production of monodisperse colloidal silica spheres: Effect of temperature," *J. Colloid. Interf. Sci.*, vol. 118, pp. 290-293, 1987.
- [47] G.H. Bogush, M.A. Tracy, C.F. Zukoski IV, "Preparation of monodisperse silica particles: Control of size and mass fraction," *J. Non-Crystal. Solids*, vol. 104, pp. 95-106, 1988.
- [48] H. Giesche, "Synthesis of monodispersed silica powders I.: Particle properties and Reaction Kinetics", *J. Eur. Ceram. Soc.*, vol. 14, pp. 189-204, 1994.
- [49] S.L. Chen, "Preparation of monosize silica spheres and their crystalline stack," *Colloid. Surface. A*, vol. 142, pp.59-63, 1998.
- [50] S.L. Chen, P. Dong, G.-H. Yang, J.-J. Yang, "Characteristic aspects of formation of new particles during the growth of monosize silica seeds," *J. Colloid. Interf. Sci.*, vol. 180, pp. 237-241, 1996.
- [51] J.H. Zhang, P. Zhan, Z.L. Wang, Y.Y. Zhang, N.B. Ming, "Preparation of monodisperse silica particles with controllable size and shape," *J. Mater. Res.*, vol. 18, pp. 649-653, 2003.

- [52] P. Ni, P. Dong, B. Cheng, X. Li, D. Zhang, "Synthetic SiO₂ Opals," *Adv. Mater.*, vol. 13, pp. 437-441, 2001.
- [53] H. Giesche, "Synthesis of monodispersed silica powders II.: Controlled growth reaction and continuous production process," *J. Eur. Ceram. Soc.*, vol. 14, pp. 205-214, 1994.
- [54] H. Míguez, F. Meseguer, C. López, Á. Blanco, J. S. Moya, J. Requena, A. Mifsud, V. Fornés, "Control of the photonic crystal properties of fcc packed submicrometer SiO₂ spheres by sintering," *Adv. Mater.*, vol. 10, pp. 480-483, 1999.
- [55] F. García-Santamaría, H. Míguez, M. Ibisate, F. Meseguer, C. López, "Refractive index properties of calcined silica submicrometer spheres," *Langmuir*, vol. 18, pp. 1942-1944, 2002.
- [56] A.A. Chabanov, Y. Jun, D.J. Norris, "Avoiding cracks in self-assembled photonic band-gap crystals," *Appl. Phys. Lett.*, vol. 84, pp. 3573-3575, 2004.
- [57] P. Jiang, J.F. Bertone, K.S. Hwang, V.L. Colvin, "Single-crystal colloidal multilayers of controlled thickness," *Chem. Mater.*, vol. 11, pp. 2132-2140, 1999.
- [58] D.J. Norris, E.G. Arlinghaus, L. Meng, R. Heiny, L.E. Scriven, "Opaline photonic crystals: How does self-assembly work?," *Adv. Mater.*, vol. 16, pp. 1393-1399, 2004.
- [59] S. H. Park, D. Q., and Y. Xia, "Crystallization of mesoscale particles over large areas," *Adv. Mater.*, vol.10, pp.1028-1032, 1998.
- [60] F. García-Santamaría, M. Ibisate, I. Rodríguez, F. Meseguer, C. López, "Photonic band engineering in opals by growth of Si-Ge multilayer shells," *Adv. Mater.* vol. 15, pp. 788-792, 2003.
- [61] L.E. Scriven, C.V. Sternling, "The Marangoni effects," *Nature*, vol. 187, pp.186-188, 1960.
- [62] Y. Jun, "Thermally stable materials for photonic band gap crystals," *Ph.D. Dissertation*, Univ. Minnesota, Minneapolis, MN, 2006.
- [63] C. Gabaldón, P. Marzal, J.B. Montón, M.A. Rodrigo "Isobaric vapor-liquid equilibria of the water + 1-propanol system at 30, 60, and 100 kPa," *J. Chem. Eng. Data*, vol. 41, pp. 1176-1180, 1996.

- [64] M.A. Kalbassl, M.W. Blddulph, "Surface tensions of mixtures at their boiling points," *J. Chem. Eng. Data*, vol. 33, pp. 473-476, 1988.
- [65] G. Vázquez, E. Alvarez, J.M. Navaza, "Surface tension of alcohol+water from 20 to 50°C," *J. Chem. Eng. Data*, vol. 40, pp. 611-614, 1995.
- [66] W. Jing, Y. Chun-Wei, T. Fang-Qiong, "Self-assembling three-dimensional colloidal photonic crystal multilayers from aqueous ethanol mixture solutions," *Chinese Phys.*, vol. 14, pp. 1581-1584, 2005.
- [67] H. Míguez, F. Meseguer C. López, M. Holgado, G. Andreasen, A. Mifsud, V. Fornés, "Germanium fcc structure from a colloidal crystal template," *Langmuir*, vol. 16, pp. 4405-4408, 2000.
- [68] O. D. Velev, T. A. Jede, R. F. Lobo, A. M. Lenhoff, "Porous silica via colloidal crystallization," *Nature*, vol. 389, pp. 447-448, 1997.
- [69] B. T. Holland, C. F. Blanford, A. Stein, "Synthesis of macroporous minerals with highly ordered three-dimensional arrays of spheroidal voids," *Science*, vol. 281, pp. 538-540, 1998.
- [70] Y. A. Vlasov, N. Yao, D. J. Norris, "Synthesis of photonic crystals for optical wavelengths from semiconductor quantum dots," *Adv. Mater.*, vol. 11, pp. 165-169, 1999.
- [71] V. N. Bogomolov, V. G. Golubev, N. F. Kartenko, D. A. Kurdyukov, A. B. Pevtsov, A. V. Prokof'ev, V. V. Ratnikov, N. A. Feoktistov, N. V. Sharenkova, "Fabrication of regular three-dimensional lattices of submicron silicon clusters in an SiO₂ opal matrix," *Technol. Phys. Lett.*, vol. 24, pp. 326-327, 1998.
- [72] C.F. Blanford, R.C. Schrodin, M. Al-Daous, A. Stein, "Tuning solvent-dependent color changes of three-dimensionally ordered macroporous (3DOM) Materials through compositional and geometric modifications," *Adv. Mater.*, vol. 13, pp. 26-29, Jan. 2001.
- [73] S.M. Yang, H. Miguez, G.A. Ozin, "Opal circuits of light—Plannarized microphotonic crystal chips," *Adv. Funct. Mater.*, vol. 12, pp. 425-431, Jun. 2002.
- [74] J.F. Galisteo-Lopex, E. Palacios-Lidon, E. Castillo-Martinex, C. Lopez, "Optical study of the pseudogap in thickness and orientation controlled artificial opals," *Phys. Rev. B*, vol. 68, pp. 115109-1-115109-8, 2003.

- [75] J.S. Foresi, P.R. Villeneuve, J. Ferrera, E.R. Thoen, G. Steinmeyer, S. Fan, J. D. Joannopoulos, L.C. Kimerling, H.I. Smith, and E.P. Ippen, "Photonic bandgap microcavities in optical waveguides," *Nature*, vol. 390, pp. 143–145, 1997.
- [76] A. Mekis, J. C. Chen, I. Kurland, S. Fan, P.R. Villeneuve, and J. D. Joannopoulos, "High Transmission through Sharp Bends in Photonic Crystal Waveguides," *Phys. Rev. Lett.*, vol. 77, pp. 3787–3790, 1996.
- [77] O. Painter, R. K. Lee, A. Yariv, A. Scherer, J. D. O'Brien, P. D. Dapkus, and I. Kim, "Two-dimensional photonic crystal defect laser," *Science*, vol. 284, pp. 1819–1821, 1999.
- [78] M. Augustin, H.-J. Fuchs, D. Schelle, E.-B. Kley, S. Nolte, A. Tunnermann, R. Iliew, C. Etrich, U. Peschel, and F. Lederer, "High transmission and single-mode operation in low-index-contrast photonic crystal waveguide devices," *Appl. Phys. Lett.*, vol. 84, pp. 663-665, Feb. 2004.
- [79] S. Noda, K. Tomoda, N. Yamamoto, A. Chutinan, "Full three-dimensional photonic bandgap crystals at near-infrared waveguide," *Science*, vol. 289, pp. 604-606, Jul. 2000.
- [80] C. Sell, C. Christensen, G. Tuttle, Z.-Y. Li, and K.-M. Ho, "Propagation loss in three-dimensional photonic crystal waveguides with imperfect confinement," *Phys. Rev. B*, vol. 68, pp. 113106-1-113106-4, 2003.
- [81] K. Busch, S. John, "Photonic band gap formation in certain self-organizing systems," *Phys. Rev. E*, vol. 58, pp. 3896-3908, 1998.
- [82] E. Palacios-Lidón, J. F. Galisteo-López, B. H. Juárez, C. López, "Engineered planar defects embedded in opals," *Adv. Mater.*, vol. 16, pp. 341-345, Feb. 2004.
- [83] W. Lee, S.A. Pruzinsky, P.V. Braun, "Multi-photon polymerization of waveguide structures within three-dimensional photonic crystals," *Adv. Mater.*, vol. 14, pp. 271-274, Feb. 2002.
- [84] Rsoft Design Group Inc., *BeamPROP 6.0 user guide*, Ossining, NY, 2005.
- [85] T. Baba, Y. Kokubun, T. Sakaki and K. Iga, "Loss Reduction of an ARROW Waveguides in Shorter Wavelength and Its Stack Configuration", *Journal of Lightwave Technology*, vol. 6, no. 9, pp. 1440-1445, Sep. 1988.
- [86] D.A.P. Bulla, and N.I. Morimoto, "Deposition of thick TEOS PECVD silicon oxide layers for integrated optical waveguide applications", *Thin Solid Films*, vol. 334, pp. 60-64, 1998.

- [87] K.N. Andersen, P.C. Nielsen, and W. Svendsen, "Silicon rich nitride thin films and waveguides", *Integrated Photonics Research*, IThA4-1, Vancouver, Canada, July 17-19, 2002.
- [88] K.-H. Schlereth, and M. Tacke, "The complex Propagation Constant of Multilayer Waveguides: An Algorithm for a Personal Computer", *IEEE J. Quantum Electron.*, vol. 26, no. 4, pp. 627-630, April 1990.
- [89] B.-H. V. Borges, M. A. Romero and Amilcar C. Cesar, "Leakage Loss Analysis in Rib Type Waveguides by the Effective Index Method", *SBMO/IEEE MTT-S IMOC'99 Proceedings*, pp.129-133, 1999.
- [90] R. G. Hunsperger, *Integrated Optics Theory and Technology*, 4th ed., Newark, DE: Springer, 1995.
- [91] R.J. Deri, E. Kapon, L.M. Schiavone, "Scattering in low-loss GaAs/AlGaAs rib waveguides", *Appl. Phys. Lett.*, vol. 51, pp.789-791, 1987.
- [92] S. A. Campbell, *The Science and Engineering of Microelectronic Fabrication*, 2nd ed., New York: Oxford Univ. Press, 2001.